Title

Photoreactivity of Ru2+ Polypyridyl Complexes Bearing the H2S–Releasing Compound GYY4137

Journal

Inorganic Chemistry, 65(20)

ISSN

0020-1669

Authors

Lotlikar, PiyushaS

Chang, Valerie

Mikhailovsky, Alexander A

et al.

Publication Date

2026-05-25

DOI

10.1021/acs.inorgchem.6c00781

Photoreactivity of Ru^{2+} Polypyridyl Complexes Bearing the H_2S-Releasing Compound GYY4137

Piyusha S. Lotlikar[1,3], Valerie Chang[1], Alexander A. Mikhailovsky[3], Joshua J. Woods[1,3], Nicholas P. Bigham[1], and Justin J. Wilson[1,3].*

[1]Department of Chemistry and Chemical Biology, Cornell University, Ithaca, New York 14853, United States

[2]Robert F. Smith School for Chemical and Biomolecular Engineering, Cornell University, Ithaca, New York 93117, USA

[3]Department of Chemistry and Biochemistry, University of California, Santa Barbara, California 93106, United States

*justinjwilson@ucsb.edu

ABSTRACT: Ruthenium (Ru) polypyridyl complexes have been extensively used as optical probes, photoactivated anticancer agents, and photocages for biologically active ligands. In this study, Ru^{2+} polypyridyl complexes were investigated as photoreleasing agents for the H_2S donor GYY4137. Four complexes of the general formula *cis*-$[Ru(NN)_2(GYY4137)]^+$, where NN = 2-2′-bipyridine (bpy), 2,2′-biquinoline (biq), 4,4′-methoxy-2,2′-bipyridine (dmobpy), and 4,4'-di-tert-butyl-2,2'-bipyridine (dtbpy), were synthesized and characterized by NMR spectroscopy and X-ray crystallography. The photochemical reactivity of these complexes was investigated, revealing that

ligand photodissociation occurs in a two-step reaction. For these reactions, long-lived intermediates where the bidentate ligands attain a monodentate coordination mode could be detected. Furthermore, the ancillary diimine ligands dictated the identity of the final photoproducts observed with some compounds ejecting GYY4137 and others ejecting the diimine ligand. Measurements of the photochemical quantum yields reveal trends in these values depending on the planarity enforced by the diimine ligands on the central complex. Density functional theory (DFT) calculations were carried out to probe the influence of complex structure on the ligand ejection process. These studies provide insight on the photoreactivity of Ru^{2+} polypyridyl complexes bearing GYY4137, results that are of relevance more broadly for the use of these scaffolds to release anionic sulfur-containing ligands.

Introduction

The biological activity of hydrogen sulfide (H_2S) has been studied extensively since its role in neuromodulation was first reported in 1996.[1] In 2005, the subsequent discovery that H_2S induces a suspended animation-like state in mice motivated further interest in exploring the therapeutic applications of this gas.[2] In humans, H_2S is now established to play an important role in signaling, joining nitric oxide (NO) and carbon monoxide (CO) as a third gasotransmitter that maintains and regulates biological processes. Among its different functions, H_2S promotes angiogenesis, mitigates oxidative stress, and attenuates inflammation in diseased tissues.[3,4] Based on these therapeutic properties, it has been investigated for the treatment of Parkinson's disease, traumatic brain injury, ischemia/reperfusion injury, cancer, and diabetes.[5–9] The use of H_2S for these applications, however, is challenging because this molecule exists as a volatile and toxic gas, rendering significant difficulties in its controlled administration at therapeutically relevant levels. To overcome these

challenges, different approaches for delivering H_2S at low concentrations suitable for biological applications have been investigated. One promising strategy uses porous solid materials to deliver H_2S in its pure gaseous form.[10–15] Prior studies using this approach have demonstrated a rapid release of H_2S, and consequently these materials need further optimization to achieve a slow sustained generation of this gas in a manner that is therapeutically valuable. Alternatively, substantial efforts on developing small-molecule H_2S prodrugs that can release this gasotransmitter under controlled conditions at physiologically relevant concentrations have been reported.[16–18] The ability to fine-tune and optimize these compounds has led to a large class of stimuli-activated H_2S donors that can be triggered by hydrolysis,[19–23] light,[24–31] thiols,[32–37] reactive oxygen species,[38–47] and enzymatic activity.[48–55] Among these compounds, light-activated prodrugs have attracted significant interest because they provide a straightforward means of spatiotemporally controlled H_2S release for either therapeutic or basic research applications.[24,25,30,31]

Notably, nearly all H_2S donors reported to date are organic molecules, even though the use of metal centers to stabilize H_2S prodrugs has potential value.[24,56] In particular, for light-activated compounds, Ru^{2+} polypyridyl complexes are highly effective photocages for a wide range of different biological molecules.[57,58] These complexes are advantageous over organic photocages because they can be excited at longer wavelengths and possess large photochemical quantum yields. This approach was previously leveraged for on-demand light-activated H_2S release.[24] In this prior study, the H_2S donor GYY4137[19] was used as a monodentate ligand, forming the complex $[Ru(tpy)(biq)(GYY4137)]^+$, where tpy = 2,2′:6′,2″-terpyridine and biq = 2,2′-biquinoline (Chart 1). This complex is stable in the dark but could release GYY4137 within 15 min upon irradiation with red light (λ = 626 nm). The free GYY4137 hydrolyzed to form H_2S, eliciting a protective effect in cells subjected to hypoxia/reoxygenation injury.

In this study, we recognized the possibility of GYY4137 to act as a bidentate ligand and sought to investigate the photochemistry of Ru^{2+} polypyridyl complexes bearing this ligand. Complexes **1**–**4**, bearing 2,2′-bipyridine (bpy), biq, 4,4′-methoxy-2,2′-bipyridine (dmobpy), and 4,4'-di-tert-butyl-2,2'-bipyridine (dtbpy)supporting ligands, were synthesized and investigated for their use as light-activated H_2S donors (Chart 1). This series of Ru^{2+} complexes was chosen to explore the effects of sterics, electronics, and structural rigidity on their photophysical properties. Our investigations demonstrate that these compounds undergo a two-step photosubstitution reaction, progressing through a long-lived photoreactive intermediate containing a monodentate GYY4317 or polypyridyl ligand. Although the photosubstitution quantum yields for this compound class were too low to be useful for their intended biological applications, this study provides a detailed investigation of their photophysical properties, yielding valuable information for the design of Ru^{2+} photocages containing sulfur-based ligands.

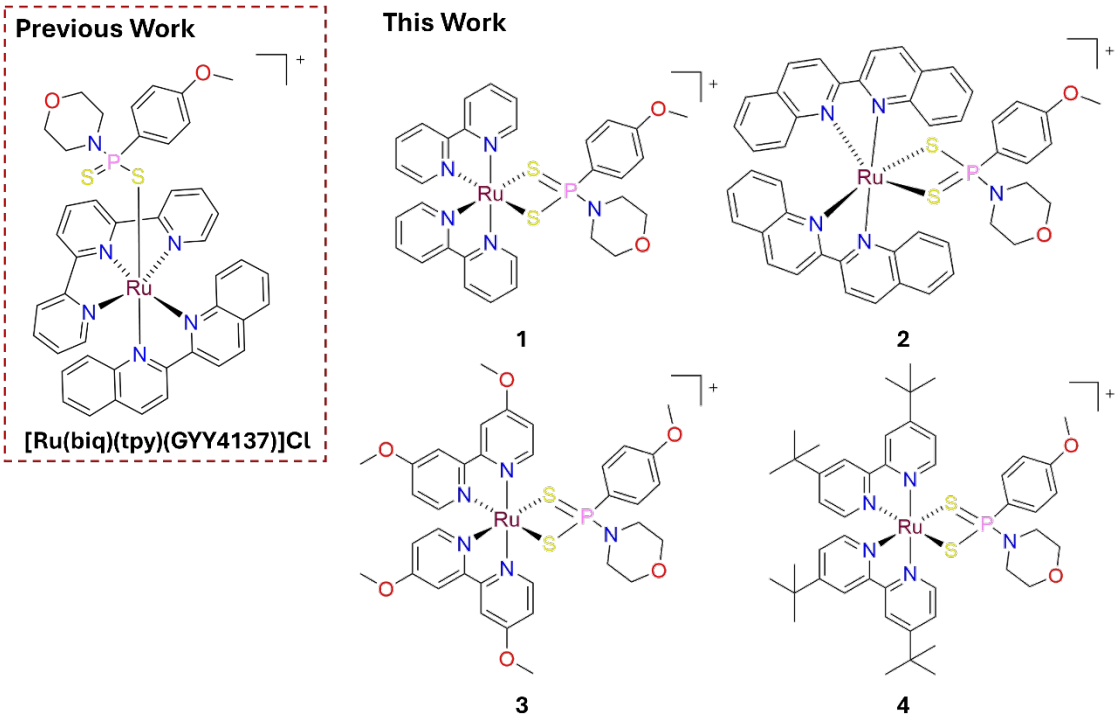

Chart 1. Structures of [Ru(biq)(tpy)(GYY4137)]Cl and compounds **1**–**4** , which were studied in this work.

Results

Synthesis and Characterization

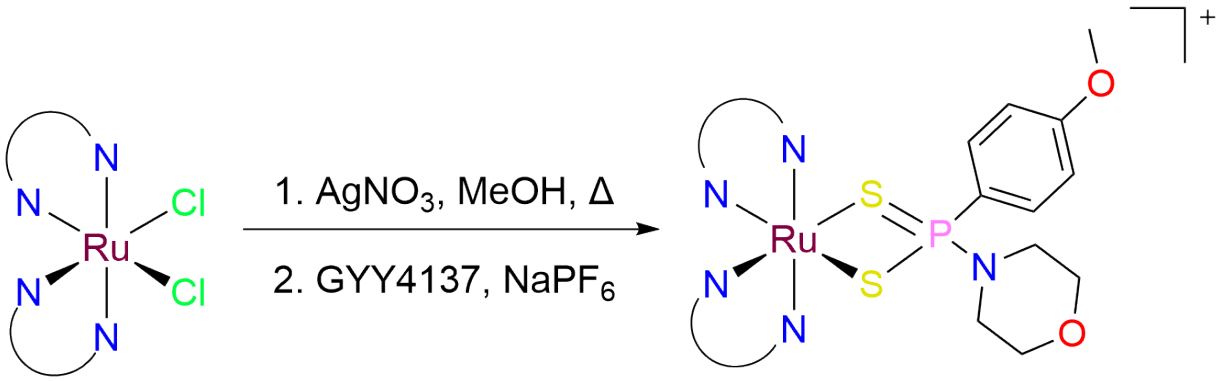

Scheme 1. Syntheses of compounds **1**–**4**.

Compounds **1**–**4** were synthesized starting from *cis*-[Ru(NN)$_2$Cl$_2$], where NN is bpy, biq, dmobpy, and dtbpy, respectively.[59,60] The precursors *cis*-[Ru(NN)$_2$Cl$_2$] were allowed to react with

$AgNO_3$ to remove inner sphere chlorides as insoluble AgCl and then treated with GYY4137 for 1 h at room temperature in methanol. Because GYY4137 can react with methanol at elevated temperatures to displace the morpholine group and afford the methoxy analogue, these reactions were maintained at room temperature to prevent this undesired side reaction.[24] Excess $NaPF_6$ was added at the end of these reactions, resulting in the precipitation of these compounds as their PF_6^- salts.

These compounds were characterized by NMR spectroscopy, mass spectrometry, UV-Vis spectroscopy, infrared spectroscopy, HPLC, and elemental analysis. Mass spectrometry results showed $[M]^+$ peaks with isotopic distribution patterns expected for Ru. The ^1H NMR resonances of the aromatic H atoms on the ligands revealed them to be asymmetric with distinct spin systems characterized for each pyridyl ring, implying a C_1 symmetry of the molecule (Figures S5, S9, S13, and S17, SI). This asymmetry is consistent with the expected bidentate coordination of the GYY4137 ligands, which enforces a cis arrangement of the polypyridyl ligands. Within their $^{31}P\{^1H\}$ NMR spectra, each compound revealed a singlet from the coordinated GYY4137 and a septet from the outer-sphere PF_6^- counterion (Figures S7, S11, S15, and S19, SI). Across the four compounds, these ^{31}P NMR resonances of the GYY4137 ligand ranged between 92–103 ppm, notably downfield from the free GYY4137 ligand that resonates at 89 ppm. Among the complexes, the $^{31}P\{^1H\}$ NMR signal of **2**, which contains the sterically demanding biq ligands, is significantly more upfield at 92 ppm. This substantial upfield shift, which is very close to that of the free ligand, may reflect a weaker interaction between the Ru center and GYY4137 in this complex, possibly due to steric crowding expected from the large biq ligands.

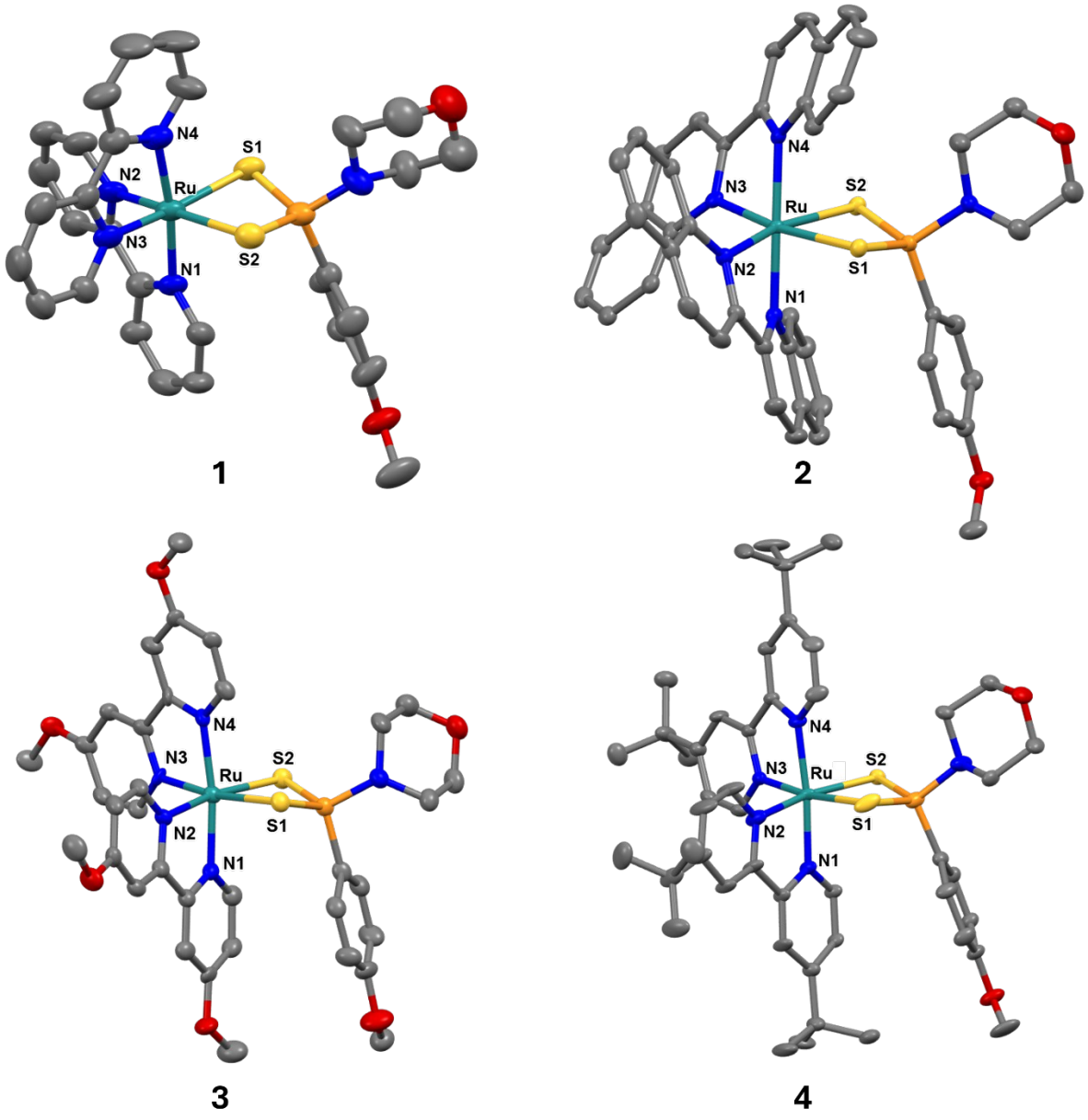

Figure 1. Crystal structures of **1**–**4**. Counterions, hydrogen atoms, and solvent molecules are omitted for clarity. Thermal ellipsoids are shown at the 50% probability level. Grey = C, red = O, blue = N, orange = P, yellow = S, and teal = Ru. Crystallographic information for all complexes is given in Table S1. Interatomic distances and angles are provided in Table 1.

Single-crystal X-ray diffraction was used to elucidate the structures of complexes **1**–**4**, which are shown in Figure 1, and to determine interatomic distances and angles, which are collected in Table 1. Consistent with the ^{1}H NMR data, all structures reveal that GYY4137 coordinates in a bidentate manner, enforcing a mutually cis arrangement of the bidentate nitrogen donor ligands. Because all of these complexes crystallized in centrosymmetric space groups, both enantiomers are present within the crystal structures. Across the four complexes, the Ru–N distances are comparable with values ranging from 2.028 to 2.097 Å. Notably, **2** exhibits the longest Ru–N distances within this group, a possible consequence of the steric crowding of the Ru center by the large biq ligands. By contrast, the Ru–S interatomic distances span a narrower range of 2.4329–2.4708 Å across the series. Furthermore, the Ru–S and P–S distances do not vary significantly within each structure, owing to equivalency of these S donors afforded by resonance delocalization of the anionic charge. The Ru–S distances are similar to those found within related Ru^{2+} complexes that also bear anionic sulfur ligands. For example, dithiocarbamate and dithiophosphinate Ru^{2+} complexes reveal Ru–S distances that span 2.41–2.43 Å.[61–63] Within $[Ru(biq)(tpy)(GYY4137)]^{+}$ and a related organometallic arene Ru^{2+} complex that both contain GYY3137 coordinating in a monodentate fashion, the Ru–S distances are 2.403–2.41 Å,[24,64] contracted by approximately 0.03 Å compared to those found in **1**–**4**. This result suggests that bidentate coordination of GYY4137 leads to weaker interactions between the Ru center and each S donor atoms.

Table 1. Selected Interatomic Distances, Angles, the Octahedral Distortion Parameters (Σ), and Ligand Torsion Angles (θ) for **1**–**4**[a]

	1	**2**	**3**	**4**
Ru–S_1 (Å)	2.445(3)	2.4430(9)	2.4329(9)	2.4445(12)
Ru–S_2 (Å)	2.459(3)	2.4708(9)	2.4366(9)	2.4389(9)
Ru–N_1 (Å)	2.047(7)	2.065(3)	2.060(3)	2.048(3)
Ru–N_2 (Å)	2.056(8)	2.071(3)	2.064(3)	2.038(3)

Ru–N_3 (Å)	2.028(8)	2.066(3)	2.071(3)	2.047(3)
Ru–N_4 (Å)	2.044(8)	2.097(3)	2.074(3)	2.064(3)
P–S_1 (Å)	2.023(3)	2.0087(12)	2.0112(12)	2.0195(14)
P–S_2 (Å)	2.016(4)	2.0086(12)	2.0317(12)	2.0091(14)
S_1–Ru–S_2 (º)	81.36(9)	80.58(3)	81.82(3)	82.55(4)
S_1–P–S_2 (º)	104.61(15)	104.55(5)	104.14(5)	106.20(6)
S_1–Ru–N_3 (º)	172.3(2)	171.19(9)	171.37(8)	172.24(9)
S_2–Ru–N_2 (º)	171.1(2)	165.46(8)	168.10(8)	169.11(9)
N_1–Ru–N_4 (º)	172.6(3)	176.35(11)	171.66(11)	174.00(13)
Σ (º)	62.89	99.72	69.20	69.67
θ (º)[b]	7.74	13.21	6.17	3.48

[a]Atoms are labeled as shown in Figure 1. Values in parentheses indicate the standard uncertainty in the last significant figure. [b] θ is the average dihedral angle between the two pyridyl groups, determined from the crystal structures as shown in Figures S1–S4, SI

Additional analysis of these crystal structures shows differing degrees of octahedral distortion at the Ru^{2+} center (Σ) and torsion angles of the polypyridyl ligands (θ). The degree of octahedral distortion was quantified using the OctaDist software package.[65] This program uses the inner-sphere atoms to calculate interatomic angles and compares how those angles deviate from the expected values within idealized octahedral and trigonal prismatic geometries. The parameter **Σ** quantifies the magnitude of this distortion, ranging from 0–270º, with smaller values of **Σ** reflecting a geometrical arrangement in line with a perfect octahedron. These **Σ** values are presented in Table 1. Although all the complexes deviate from perfect octahedral geometry, **1** is the least distorted (**Σ** = 62.89°), whereas compounds **3** and **4**, which contain ligands bearing substituents in the para positions of the pyridyl ligands, have higher **Σ** values of 69.20 and 69.67°, respectively. Further steric congestion, observed in the expanded biq ligand within compound **2**, resulted in a significant distortion from octahedral geometry, corresponding to a **Σ** value of 99.7°.[66] Further, the planarity of the ancillary ligand was probed by measuring the dihedral angle (θ) between the planes defined by the each pyridine ring of one diimine ligand (Figures S1–S4, SI).[67] The mean values of θ, as

measured from the structural data, were found to be 7.74, 13.21, 6.17, and 3.48°, for **1**–**4**, respectively.

Photophysical Properties

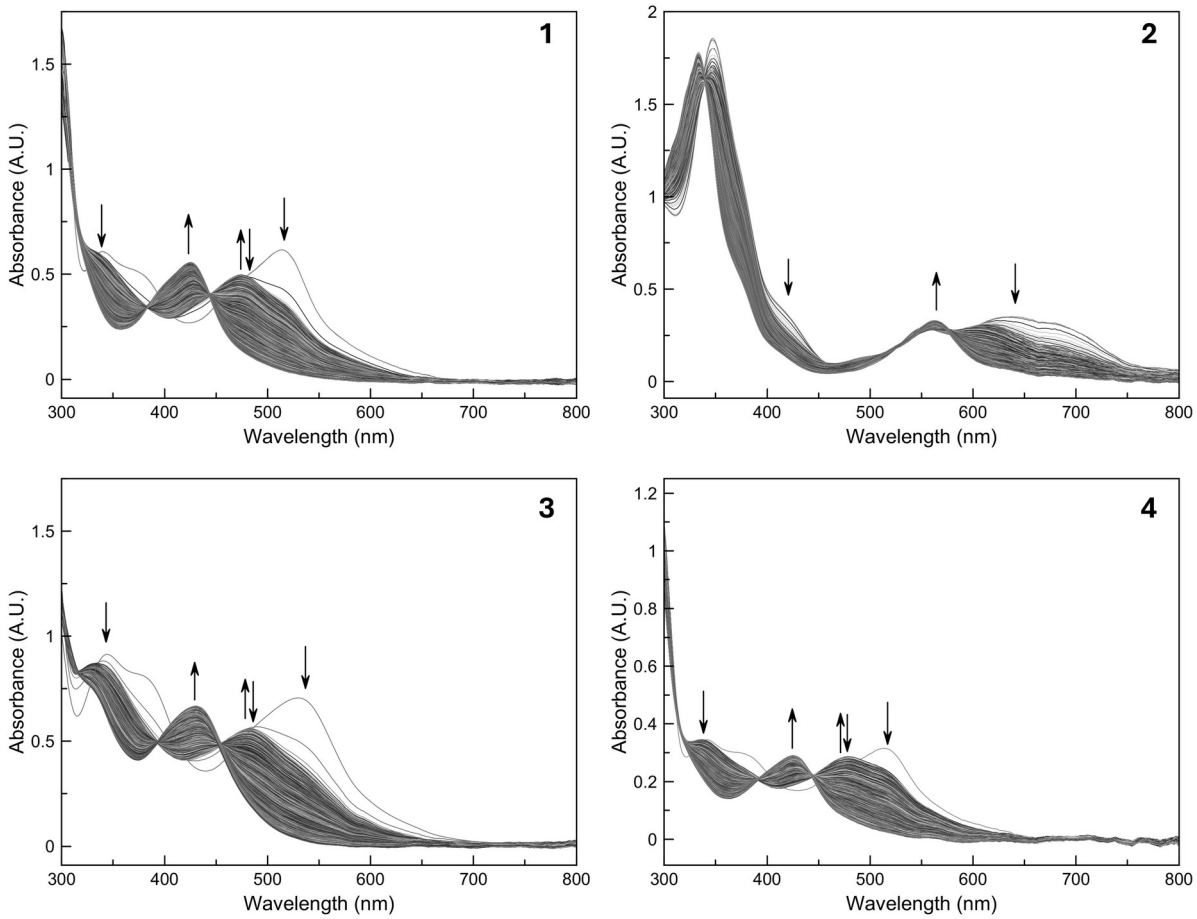

Figure 2. Changes in the electronic absorption spectra of **1**–**4** in MeCN under 470 nm light irradiation (photon flux = 4.55×10^{-5} mol s^{-1} dm^{-4}, t_{irr} = 17.75 h, Δt_{irr} = 30 s, T = 298 K).

The electronic absorption spectra of the compounds was measured in acetonitrile (MeCN). Each spectrum features high-energy absorbance bands, arising from π–π* transitions on the polypyridyl ancillary ligands. Intense lower-energy transitions above 500 nm were observed, corresponding to metal-to-ligand charge transfer (MLCT) transitions. Among the complexes in the series, **2** featured the lowest-energy MLCT transitions (λ_{max} = 639 nm), presumably due to the extended π delocalization of the biq ligand. Compound **3** exhibited the lowest energy MLCT band of the bipyridine-based ligands (λ_{max} = 529) because of the electron rich nature of the dmobpy ligand that raises the energy of the occupied Ru-based orbitals, thereby decreasing the energy gap between occupied Ru orbitals and vacant dmobpy-based orbitals.

The photochemistry of these compounds in MeCN was investigated by UV-Vis spectroscopy. Upon irradiation of the compounds with 470-nm light, their initial low-energy MLCT bands decayed rapidly, over a 1–3 min time period, resulting in the appearance of a slightly blue-shifted absorbance band. Upon further prolonged irradiation over 17.5 h, the spectra continued to evolve, revealing the ingrowth of new higher-energy absorbance features (Figure 2 and S38–41, SI). The absorbance bands of the final photoproducts are blue-shifted relative to the initial MLCT bands by 100–200 nm or approximately 5000 cm^{-1}. To confirm that the changes in the UV-Vis spectra arose from light rather than thermal reactions, these solutions were heated in the dark at 37 °C and analyzed by both UV-Vis and NMR spectroscopy. This analysis showed that there were no spectral changes under these conditions (Figures S25–S32, SI), confirming that these reactions are driven exclusively by light. In addition, incubation of these solutions with an H_2S-responsive dye produced no turn-on of fluorescence, further confirming that direct H_2S release from the coordinated GYY4137 is not occuring either. Light irradiation likewise failed to achieve H_2S relase in these conditions, most likely refelcting the inability of GYY4137 to hydrolyze in MeCN (Figures S33–34, SI).

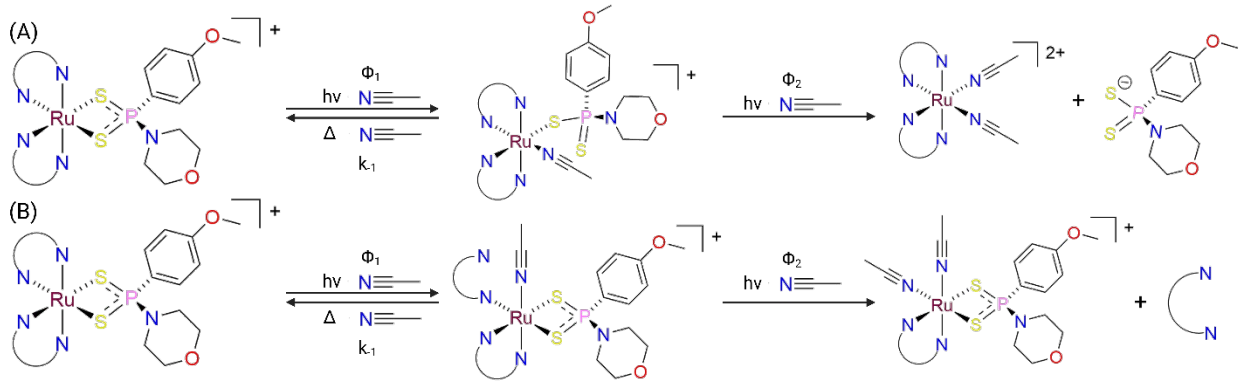

Scheme 2. Schematic representation of the loss of either GYY4137 via the formation of a (A) $[Ru(NN)_2(\kappa^1\text{-GYY4137})(MeCN)]^+$ or (B) the polypyridyl ligand via the formation of $[Ru(NN)(\kappa^1\text{-NN})(GYY4137)(MeCN)]^+$.

The observation of a fast photochemical transformation, followed by a much slower one, suggests that the photochemistry of this compound class is proceeding in two distinct steps. To further characterize this process, the photoreactions were monitored by LC-MS (Figures 3 and S35, SI). Analysis of samples that had been irradiated for 30 min revealed the presence of new signals on the chromatogram, which have *m/z* values of 742.9, 862.8, and 484.1for **1**, **3**, and **4**, respectively. These *m/z* values correspond to the $[M + MeCN]^+$ and $[M + MeCN + H]^{2+}$ molecular ion peaks, suggesting that an MeCN ligand is present within the Ru^{2+} coordination sphere. Given the strong preference for six-coordinate octahedral geometries by Ru^{2+} and related d^6 low-spin transition metal centers,[68] these molecular ion peaks most likely arise from the formation of an intermediate that has one of its ligands bound in a monodentate fashion, as $[Ru(NN)_2(\kappa^1\text{-GYY4137})(MeCN)]^+$ or $[Ru(NN)(\kappa^1\text{-NN})(GYY4137)(MeCN)]^+$. At much longer time points in the photoreaction, new peaks within the chromatogram arise with *m/z* values that correspond to the molecular ion peaks for $[Ru(NN)(GYY4137)(MeCN)_2]^+$, ($[M - NN + 2\ MeCN]^+$) and $[Ru(NN)_2(MeCN)_2]^{2+}$ ($[M - GYY4137 + 2\ MeCN]^{2+}$). Based on these data, the two-step photoreaction in Scheme 2 is proposed. The observation of polypyridyl versus GYY4137 release during these photoreactions depends on the specific complex. For example, LC-MS analysis of the photoreaction of **2**, for which no detectable intermediates were observed, revealed the final products of his process to be the free biq ligand (*m/z* = 256.3) and $[Ru(biq)(GYY4137)(MeCN)_2]^+$ (*m/z* = 686.8) (Figure 3). For the other compounds, slightly different product distributions were observed upon completion of photolysis. The major species that arise as the final products of the photoreaction of **3** and **4** are GYY4137 and $[Ru(NN)_2(MeCN)_2]^{2+}$ ($[M - GYY4137 + 2\ MeCN]^{2+}$), which were characterized by *m/z* values of 307.8 and 360.1, respectively (Figures 3 and S35, SI). By contrast, the complete photolysis of **1**

revealed two products, $[Ru(bpy)_2(MeCN)_2]^{2+}$ and $[Ru(bpy)(GYY4137)(MeCN)_2]^{+}$, which are highlighted in blue and purple, respectively, within the chromatograms shown in Figure 3. For this complex, the ratio of these products is 9:1, as determined via the integrated area of each peak on the absorbance chromatogram. These results demonstrate that photolysis can proceed through ejection of either the GYY4137 or diimine ligand in a manner that is dependent on the supporting ligands of these complexes.

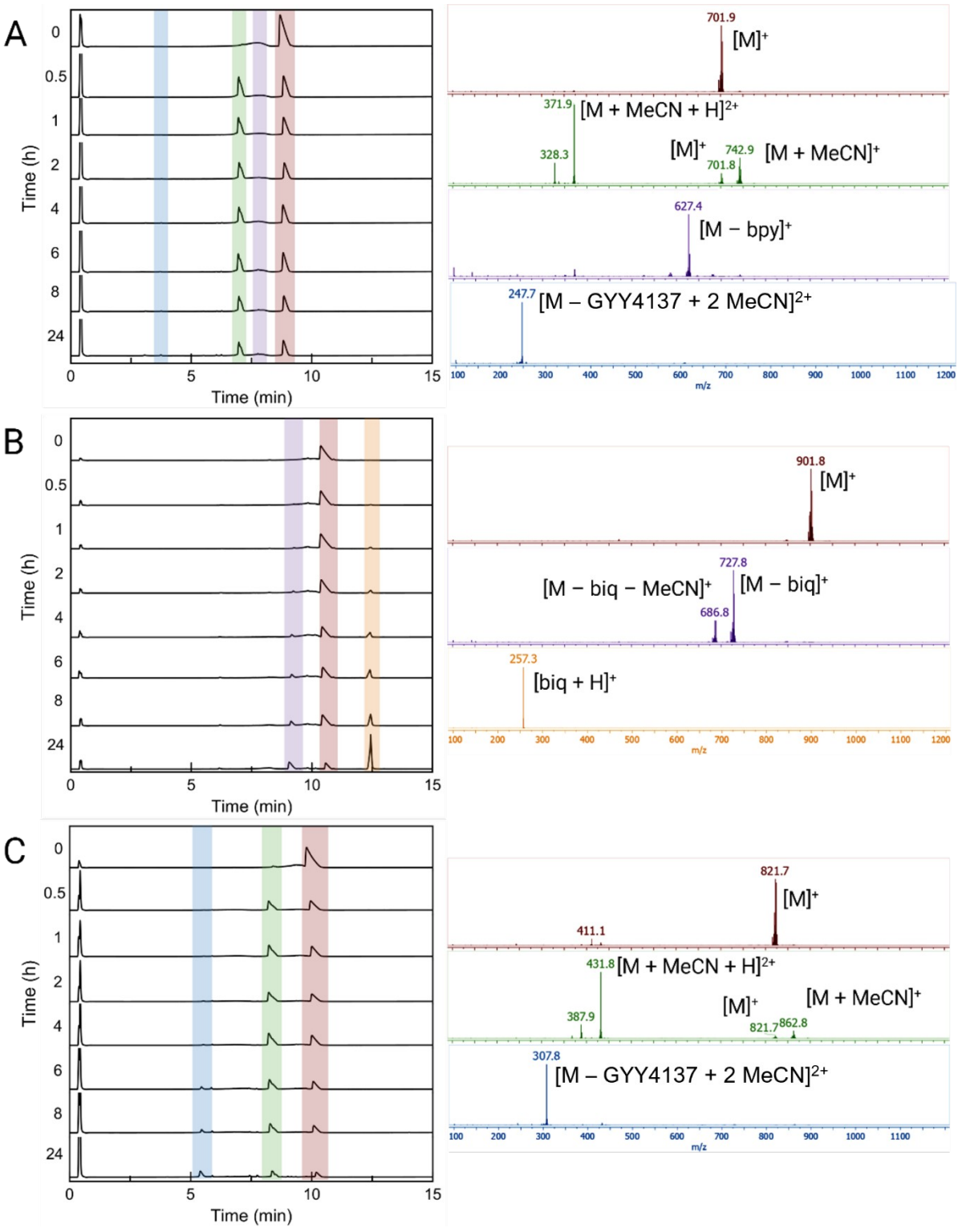

Figure 3. Liquid chromatograms and mass spectrometry traces showing the reactivity patterns of **1** (A), **2** (B), and **3** (C). Those for compound **4**, which are similar to the data obtained for **3**, are shown in Figure S35, SI. The peaks in the chromatogram are highlighted in different colors that corresponds to the mass spectra of the same color shown to the right. $[M]^+$ is defined as $[Ru(NN)_2(GYY4137)]^+$.

As noted above, all of the photoreactions proceed in two steps. Consequently, the quantum yields were determined by fitting the UV-Vis spectral evolution data to a series of differential equations that describe the changes in concentration over the irradiation period.[69] This analysis allows for the determination of the quantum yield of the first step (Φ_1), which leads to the formation of a monodentate intermediate, as well as the quantum yield of the second step (Φ_2), which describes the complete dissociation of the ligand from the monodentate intermediate (Scheme 2). The quantum yields Φ_1 and Φ_2 were calculated by Eq. 4 using the iteratively calculated concentrations of each species as found in Eqs. 1–3. As shown in Eqs. 1 and 2, these series of differential equations also account for the reverse thermal reaction, which proceeds with a first order rate constants of k_{-1} in a photon-independent manner. This rate constant was determined independently, as described in the following section, and applied as a fixed constant for this data fitting analysis. The first quantum yield Φ_1 ranged from 1.3–4 × 10^{-2} for these compounds. Complex **4** exhibited the largest Φ_1 value (4 × 10^{-2}, respectively) within the series. The Φ_2 values, which ranged from 0.0.72–2× 10^{-4}, are smaller by two to three orders of magnitude than Φ_1, reflecting the relative inefficiency of the complete ligand photodissociation.

Table 2. Summary of Spectroscopic and Photophysical Properties of Complexes **1**–**4**

	1	**2**	**3**	**4**
^{31}P δ (ppm)	103.06	92.17	103.06	101.74
λ_{MLCT} (nm)	513	639	529	513
k_{-1} (s^{-1} × 10^{-5})[a]	5.08 ± 0.27	61.4 ± 8.3	5.22 ± 0.13	7.11 ± 0.17
Φ_1 (× 10^{-2})[a]	2.7 ± 0.3	1.3 ± 0.2	3.50 ± 0.07	4 ± 1
Φ_2 (× 10^{-4})[a]	0.72 ± 0.03	4 ± 1	1.05 ± 0.08	2.0 ± 0.6

[a] Photochemical quantum yields and first order rate constants defined for the reactions in Scheme 2.

Thermal Rechelation

As noted above, the monodentate intermediate has the potential to thermally revert to the starting material, which was accounted for in the analysis and data fitting to determine the quantum yield values. We investigated this process by irradiating the samples for a brief period to maximize formation of this intermediate, and then monitoring their UV-Vis spectra as they thermally reequilibrated in the dark at 25 °C. The UV-Vis spectra showed that the blue-shifted absorbance band of the intermediate evolved into the MLCT absorbance bands of the starting material. An analysis of the time-dependent increase in intensity of the starting materials MLCT band via an integrated first order rate law afforded the rate constants (k_{-1}) of 5.08, 61.4, 5.22, and $7.11 \times 10^{-5}\ s^{-1}$ for **1**–**4**, respectively (Table 2, Figures S47–S50, SI). These values were used within the quantum yield measured described in the section above. Of note, the k_{-1} of **2** ($6.1 \times 10^{-4}\ s^{-1}$) is over an order of magnitude larger than those of the other complexes. Although rate constants for the rechelation of bidentate dithiophosphinates have not been previously measured, the light-induced formation and subsequent thermal reversion of monodentate diimines on Ru^{2+} centers have been studied.[70,71,72]

Density Functional Theory (DFT) Calculations

DFT calculations were used to gain a better understanding of the ligand dissociation processes of these compounds. DFT calculations were performed using *Gaussian 16*[73] with the PBE1PBE functional.[74] The LANL2DZ basis set and effective core potential, as well as the 6-31G(d,p) basis set, were employed for Ru and the light atoms, respectively.[75,76] The SMD solvation model was applied to account for solvent effects.[77] The complexes were optimized in the singlet ground state, affording structures with similar interatomic distances and angles as those found in the crystal structures. Similarly, the geometries of the photochemical intermediates, [Ru(NN)$_2$(κ^1-

GYY4137)(MeCN)]$^{+}$ and [Ru(NN)(κ^{1}-NN)(GYY4137)(MeCN)]$^{+}$ and photoproducts [Ru(NN)$_2$(MeCN)$_2$]$^{2+}$ and [Ru(NN)(GYY4137)(MeCN)$_2$]$^{+}$ were optimized. The optimized geometries of the intermediates are shown in Figure 4. The structural distortions present in [Ru(NN)$_2$(κ^{1}-GYY4137)(MeCN)]$^{+}$ intermediates are not significant and show expected changes in the coordination sphere to accommodate a new inner-sphere acetonitrile ligand. By contrast, [Ru(NN)(κ^{1}-NN)(GYY4137)(MeCN)]$^{+}$ for complexes **1**–**4** show a significant change in the torsion angle between the two pyridyl groups (Table S4). This distortion rotates the uncoordinated pyridyl group to accommodate the additional inner-sphere acetonitrile. These structural differences are expected to contribute to the relative stabilities of these monodentate intermediates.

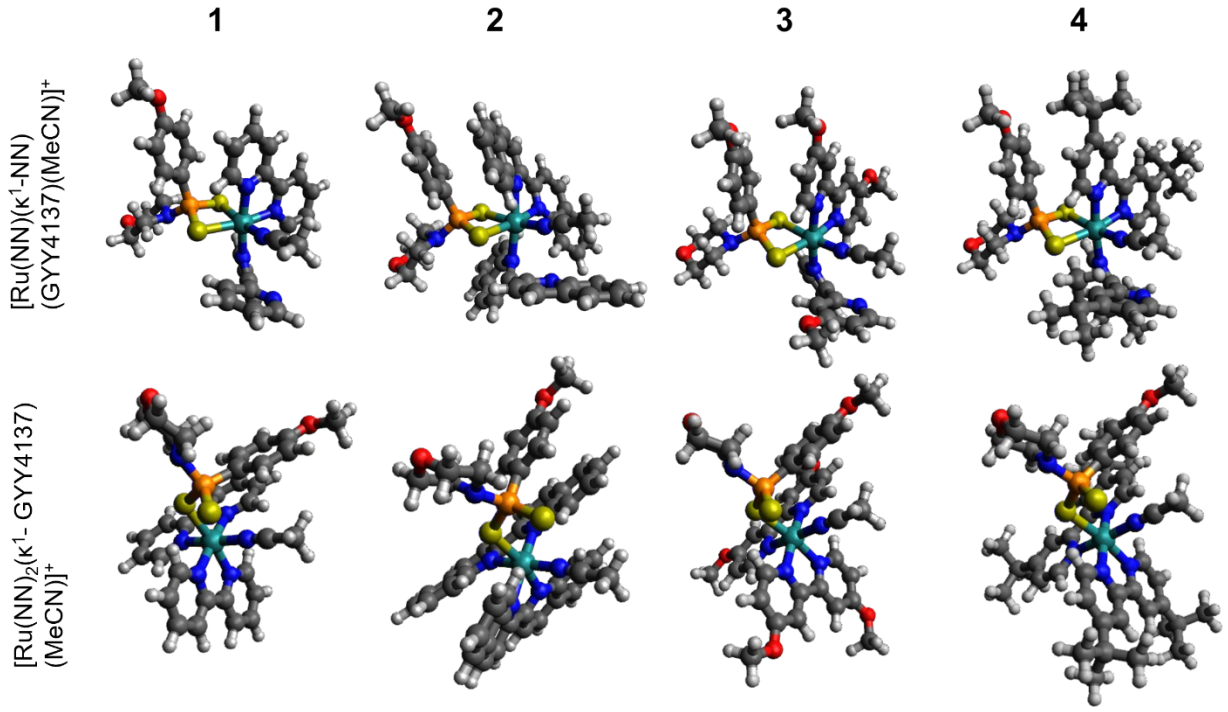

Figure 4. DFT-optimized structures of monodentate N (mono N) and monodentate S (mono S) intermediates of **1**–**4** resulting from dechelation of GYY4137 or one polypyridyl ligand, respectively.

The Gibbs free energies of the starting complexes, intermediates, and products, all performed in the singlet ground state, were calculated and used to approximate the potential energy landscape of the thermodynamic processes associated with ligand loss, as shown in Figure 5. For all complexes, the full dissociation of either the GYY4137 or the diimine ligand is thermodynamically unfavorable, as reflected by the high thermal stability in solution. Notably, for all complexes, loss of GYY4137 is substantially less energetically uphill compared to loss of the diimine ligand. This energy difference, however, is smaller in magnitude for complex **2**, the complex bearing the biq ligand. Furthermore, the monodentate intermediates along the pathway for GYY4137 photodissociation are also significantly lower in energy than the monodentate intermediates leading to diimine dissociation. These results suggests that thermal loss of GYY4137 should be the preferred pathway, and is reflected in the selectivity patterns observed.

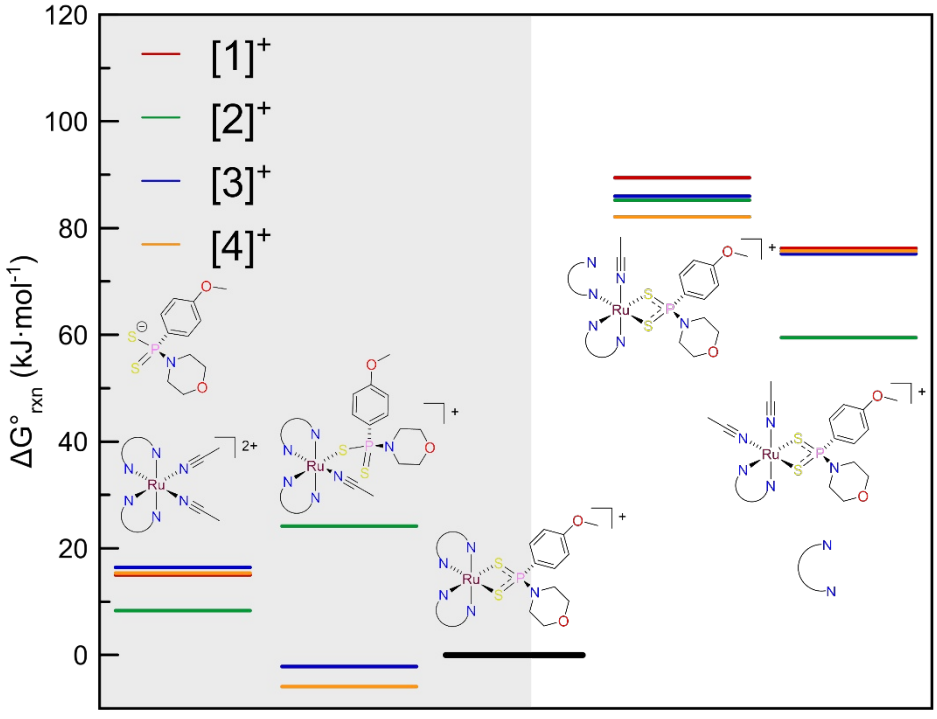

Figure 5. Comparison of the Gibbs free energy for ligand dissociation steps involving sulfur ligand loss (left) and loss of a diimine ligand (right). The free energies are relative to the starting complexes. The free energy calculations are based on ground state singlet structural calculations.

In order to garner a better understanding of the photophysical properties of these complexes, we turned to time-dependent DFT calculations. TD-DFT calculations were carried out at the ground state geometries of **1**–**4** to calculate the lowest 30 singlet excited states. Although there were some deviations, the calculated singlet excited state energies were in fairly good agreement with the experimental absorbance spectra (Figures S51–S54, SI). Electron density difference maps were employed to determine the character of the major low-energy transitions (Figures S55–58, SI). The S_1 state for all complexes was found to be of HOMO → LUMO ^{1}MLCT character. Likewise, the subsequent four higher energy singlet excited states (S_2–S_5) for complexes **1**–**4** are also ^{1}MLCT in character. High oscillator strength transitions centered around 350 nm for complexes **1**–**4** represent $\pi \rightarrow \pi^*$ transitions within the diimine ligands.

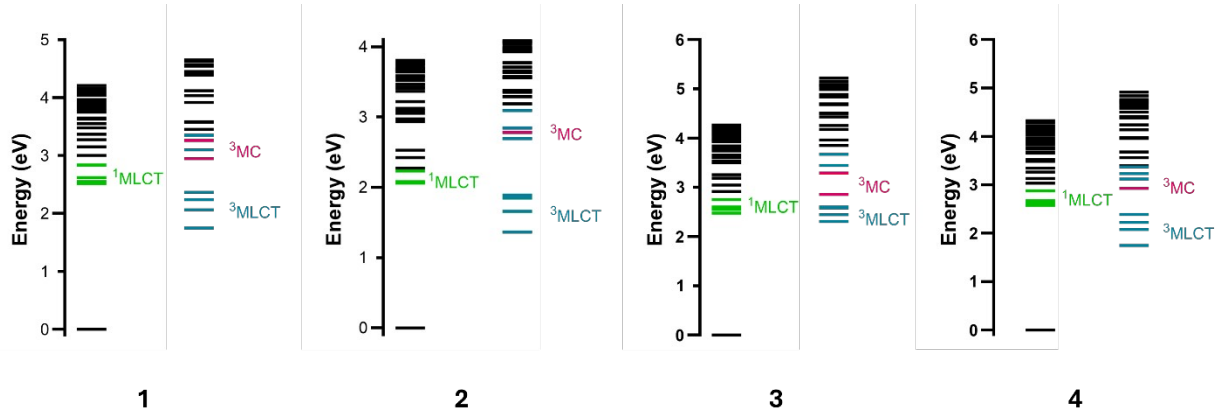

Figure 6. Jablonski diagrams, as calculated from TD-DFT, for compounds **1**–**4** depicting the key calculated states, including ^{1}MLCT (green), ^{3}MLCT (teal) and ^{3}MC (fuchsia) states.

The lowest-energy triplet excited states were optimized, and T_1 states were found to be 1.75, 1.36, 2.31, and 1.73 eV above S_0 for **1**–**4**, respectively. Spin density plots reveal unpaired electrons to reside on both the metal center and the diimine ligands, indicating that these states correspond to

the lowest-energy ^{3}MLCT states (Figures S59–62, SI). From these triplet states, TD-DFT was used to calculate the energies of higher-lying triplet excited states and from these states spin density plots were generated aid in their characterization. T_1–T_4 were determined to be ^{3}MLCT in nature for **1**–**4**. A sole ^{3}MC state was observed for **2** and **4** and found to be T_6 and T_5, respectively. For **1** and **3**, the two ^{3}MC states were to be T_5 and T_7 for **1** and T_5 and T_6 for **3.** A summary of these calculated states are presented in Figure 6.

Discussion

A series of complexes bearing the phosphinodithioate ligand GYY4137 were synthesized and characterized for use as light-activated H_2S donors. The NMR spectra and X-ray crystal structures of these complexes reveal the formation of all complexes with the expected bidentate coordination of GYY4137. An analysis of the crystal structures of **1**–**4** provides valuable insights into the effects of the ligands on the coordination environment of the central Ru^{2+} ion. The distortion from octahedral geometry, as determined from the OctaDist program, reveals that **2** deviates substantially from this ideal geometry. The distortion parameter Σ for this complex is 99.72°, substantially larger than those of the other complexes, which only span values ranging from 62.82–69.67°. This large distortion has previously been noted within other Ru^{2+} complexes of biq and has been leveraged to increase the photochemical quantum yields for ligand dissociation within this compound class.[24,66,78–80] GYY4137 has previously been used as a ligand for Ru^{2+} complexes.[24,64] In both of these prior structures, the GYY4137 was bound in a monodentate fashion. The Ru–S distances within **1**–**4**, in which GYY4137 is bound in a bidentate manner, are notably longer than the monodentate GYY4137 complexes by approximately 0.05 Å. The elongated Ru–S distances are most likely a consequence of weaker ionic interactions due to delocalization of charge

between the two sulfur atoms. In comparing inner-sphere Ru–N and Ru–S lengths among complexes **1**–**4**, the biq-containing complex **2** displayed the longest Ru–S and Ru–N distances, with values of 2.443 and 2.4708 Å for Ru–S interactions and 2.065, 2.071, 2.066, and 2.097 Å for Ru–N interactions. The longer distances within **2** most likely arise from the higher steric congestion due to the large biq ligand. The significant structural distortion within **2** is also apparent within its ^{31}P NMR spectrum. For **1**, **3**, and **4** their ^{31}P chemical shifts range between 101.74–103.06 ppm. By contrast, ^{31}P chemical shift of **2** is shifted upfield to 92.17 ppm, which may reflect weaker interactions of this ligand with the Ru^{2+} center. For comparison, the monodentate GYY4137 in $[Ru(biq)(tpy)(GYY4137)]^{+}$ and an organometallic Ru^{2+} arene complex with this ligand feature similarly upfield-shifted ^{31}P NMR chemical shifts of 98.93 and 91.0 ppm, respectively, indicating that this spectroscopic parameter may be sensitive to the nature of this metal-ligand interaction.

The analysis of the photochemistry of this compound class by UV-Vis spectroscopy reveals that they all undergo an initial fast photochemical reaction, generating a long-lived intermediate that exhibits a much slower subsequent photolysis. Based on the LC-MS data and literature precedence,[72,81–83] the intermediate can be identified to be a species in which one of the ligands is bound in a monodentate manner. The formation of these photochemical intermediates, which arise from dissociation of one of the donor atoms of the bidentate ligand, has been observed in many related Ru^{2+} polypyridyl systems bearing three bidentate ligands.[72,84] Within these systems, a Ru^{2+} polypyridyl complex formed a reactive and short-lived photochemical intermediate that appeared rapidly at the onset of irradiation and was susceptible to further decomposition upon continued irradiation to fully release one of the bidentate ligands. Furthermore, if the intermediate is not

subjected to further photolysis, this species reverts to the starting material, a process that is consistent with rechelation of the bidentate ligand.

In the context of sulfur-containing ligands, the photochemistry of **1**–**4** can best be compared with a class of Ru^{2+} polypyridyl complexes bearing bidentate bisthioether ligands.[85–87] For these bisthioether complexes, the initial photosubstitution reaction, which resulted in the change of thioether coordination mode from bidentate to monodentate, proceeded within several minutes (Φ_1 = 0.16–0.25). For the second photosubstitution, which leads to complete dissociation of the thioether, prolonged irradiation times, on the order of hours, were required due to the smaller quantum yields for this step (Φ_2 = 0.0055–0.0093). Complexes **1**–**4** exhibit similar photochemical reactivity, where Φ_1 = 0.013–0.04 and $\Phi_2 = 0.72–4\times10^{-4}$. Importantly, the reactivity across the series varied somewhat. Photolysis of compounds **3** and **4** liberates the GYY4137 ligand, whereas compound **2** releases the biq ligand. Irradiation of compound **1** triggers primarily the dissociation of GYY4137 but also releases small quantities of bpy ligand. The quantum yields of these first photochemical steps are similar to those within the thioether systems. By contrast, the second step, which leads to full ligand dissociation for **1**–**4**, proceeds with much smaller quantum yields, requiring up to 18 h under our irradiation conditions for completion. Although a decrease in Φ_2 by two orders of magnitude from Φ_1 was observed for the bisthioether complexes, the disparities between Φ_1 and Φ_2 for **1**, **3**, and **4** are an order of magnitude larger, indicating that there are important differences between these systems. First, GYY4137 is anionic, whereas the bisthioether ligands are neutral. The charge on GYY4137 most likely leads to a significant electrostatic stabilization between it and the cationic Ru^{2+} center, contributing to its substantially less efficient photodissociation. Another important factor is the chelate-ring size of the departing ligand. For **1**–**4**,

the GYY4137 ligand makes a rigid four-membered chelate ring. By contrast, the bisthioether ligands in the previously studied complexes form flexible five-membered chelate rings. Thus, rechelation of monodentate GYY4137 is more favorable due to the lower entropy of the monodentate intermediate, leading to the substantially smaller effective Φ_2 values.[88] In this comparison of Φ_1 and Φ_2 values, it should be noted the difference between these two values for **2** is only two orders of magnitude, comparable to those of the bisthioether complexes. Furthermore, the Φ_2 of **2** is similar in magnitude of to the quantum yields of relate Ru^{2+} polypyridyl complexes that release their diimine ligands.[89] These results are consistent with the fact that **2** ejects the neutral biq ligand, instead of the anionic GYY4137 ligand, upon photoirradiation.

For **1**, **3**, and **4** that eject GYY4137, the photochemical quantum yields vary slightly. For example, the first photochemical reaction of **4** proceed with a quantum yield of 4%. By contrast, **1** and **3** exhibit smaller quantum yields of 2.7 and 3.50%, respectively. This efficiency of the initial photoreaction (Φ_1) appears to relate to the rigidity and steric effects of the supporting diimine ligands. In the case of **4**, measurements of the angles between planes of the linked pyridyl donors reveal a nearly planar diimine surface where θ was measured as 3.48° for **4.** Notably larger dihedral angles are present within **1** and **3** (Table 1). In this context, correlations between photochemical quantum yields and supporting ligand rigidity and planarity within related Ru polypyridyl complexes have been observed,[90] and similar effects may be in operation within the current system. Another feature that influences photosubstitution quantum yields in Ru complexes is their degree of distortion from ideal octahedral geometries. As the geometry distorts, photodissociative ligand field excited states become lower in energy, allowing for efficient population of this state via an initial excitation to the MLCT state. We found that despite the moderate increase of Φ_1, the values of the

distortion parameter of **4** was similar in magnitude to that of **3**, with a marginal change of 0.47° between them. The higher quantum yield of **4** is, therefore, contrary to the conventional understanding of the relationship between Φ and octahedral distortion. The octahedral distortion parameter of **4** is 69.67°, similar to those of **1** and **3**, each valued at 62.89° and 69.20°, respectively. With minimal differences between them, octahedral distortion appears to have only a minor effect on the quantum yields for ligand release from this compound class.

Because Φ_2 is significantly smaller than Φ_1, the photogenerated intermediates bearing monodentate GYY3147 or diimine ligands accumulate in high concentrations. Consequently, upon cessation of irradiation, these intermediates can reconvert thermally back to starting materials via reformation of the bidentate coordination mode. The ability of monodentate intermediates of other photoactive Ru^{2+} systems to revert back to starting material once irradiation has stopped has previously been observed.[89] The first order rate constants for this rechelation process show a dichotomy between those for compounds **1**, **3**, and **4**, which primarily release GYY4137 through an intermediate where this ligand attains a monodentate coordination mode, and **2**, which releases the biq ligand presumably through a similar N-bound monodentate intermediate. For **1**, **3**, and **4**, the rate constants at 25 °C are 5.08, 5.22, and 7.11×10^{-5} s^{-1}, substantially smaller than the 61.4×10^{-5} s^{-1} rate constant of **2**. Notably, this rechelation rate constant for **2** is similar to that of $[Ru(bpy)_2(dmbpy)_2]^{2+}$ (dmbpy = 3,3'-dimethyl-2,2'-bipyridine), where k_{-1} is 0.0001 s^{-1} in MeCN at 25 °C.[89] The faster rechelation of monodentate biq in **2** compared to monodentate GYY4137 in **1**, **3**, and **4** is somewhat unexpected given the more favorable charge and chelate ring size for reattachment of GYY4137. Lastly, a rough inverse correlation between the rechelation rate constant

k_{-1} and Φ_2 is apparent. This correlation makes sense because rechelation of the monodentate ligand is in competition with its complete photodissociation from the inner sphere.

Our analysis of the photochemical product distribution by LC-MS within **1–4** revealed some key differences. For compounds **3** and **4**, the major photoproducts arise from the release of the GYY4137 ligand. With **1**, release of the bpy diimine ligand was observed as a minor photoproduct, whereas for **2,** ejection of the biq diimine ligand was the major photoproduct. This product distribution can be partly explained by analysis of the DFT-optimized geometries of the monodentate N species, which are the intermediates on pathway to complete diimine ligand dissociation. These optimized geometries show rotation about the C–C bond linking the two pyridyl groups. This rotation moves the N donor atom away from the Ru^{2+}, an orientation that is required to prevent reassociation. Consequently, the absence of substituents on the bpy ligands of **1** make this reorganization more sterically accessible for the other ligands that contain *para* substituents. Likewise for **2**, the two biq ligands induce such a large degree of octahedral distortion that its release is favored to relieve the strain on the molecule. These results can partly explain the observation of diimine dissociation found exclusively from the photoreactions of **1** and **2**. However, the DFT results, which were calculated exclusively for ground states, should be used with caution when extrapolated for the photochemical processes, which proceed through excited states.

TD-DFT calculations were employed to obtain a clearer picture of the photochemical excited states that dominate the reactivity of Ru polypyridyl complexes. Energies of excited state singlets and triplets were obtained from calculations of the vertical excitation from the lowest energy singlet and triplet states. These data suggest that initial excitation via 470 nm blue light populates ^{1}MLCT states, which undergo intersystem crossing and internal conversion to facilitate

ligand dissociation via low energy ^{3}MC states. Like many other Ru^{2+} polypyridyl complexes, the dissociative ^{3}MC states are higher-lying than ^{3}MLCT states of **1**–**4**, , suggesting that thermal contributions facilitate the transition between these potential energy surfaces. Compounds **2** and **4** have a sole low-lying ^{3}MC state, which is in agreement with the observed single pathway of ligand loss, involving the loss of biq and GYY, respectively. The existence of multiple ^{3}MC states, T_5 and T_7, belonging to **1** may reflect the multiple dissociative pathways available to this compound that may lead to different ligand dissociations. The limitations of this approach, however, are evident in the consideration of compound **3**, which also features two ^{3}MC states, T_5 and T_6, separated by an energy of 0.43 eV. A more comprehensive study, beyond the scope of this current work, of the potential energy surfaces of these triplet excited states would be required to glean a more meaningful result from these findings.

Summary

In this study, we prepared a series of Ru^{2+} polypyridyl complexes bearing the H_2S donor GYY4137. Our detailed investigation of their photochemistry revealed the supporting polypyridyl ligands to play a large role in dictating the observed photoproducts and the overall efficiency of the photoreactions. Examination of the excited states of these compounds suggest the importance of ^{3}MC states in the dissociative pathways presented. Given the small quantum yields for these compounds, they will most likely not be useful for therapeutic H_2S release. In any case, this compound class provides additional insight and data on the use of bidentate anionic sulfur-containing donors as ligands for photoactive Ru^{2+} polypyridyl complexes. Our DFT analysis reflects the complexity of both the excited and ground state potential energy surfaces for this compound class, highlighting how factors like sterics can drive the dissociation of ligands conventionally

considered to be spectators. Furthermore, this DFT analysis also relays the importance of sterically bulky *para*-substituents that are removed from the immediate Ru^{2+} coordination sphere , which act to alter diimine ligand planarity to modulate their photodissociation.

Experimental Section

Reagents and Materials

All reagents were obtained commercially and used without further purification. $[Ru(bpy)_2Cl_2]$, $[Ru(biq)_2Cl_2]$, $[Ru(dmobpy)_2Cl_2]$, and $[Ru(dtbpy)_2Cl_2]$were prepared as previously described.[59,60]

Physical Measurements

1D-NMR (^1H, $^{13}C\{^1H\}$, and $^{31}P\{^1H\}$) spectra were acquired at 25 ºC on a 500 MHz Bruker Avance NEO spectrometer equipped with a Prodigy CryoProbe (Bruker, Billerica, MA). Chemical shifts were referenced to solvent peaks in ^1H and $^{13}C\{^1H\}$ NMR spectra, relative to tetramethylsilane at $\delta = 0.00$ ppm. A solution of $NaPF_6$ in D_2O was used as the reference for $^{31}P\{^1H\}$ NMR spectra, setting the chemical shift of this compound to be $\delta = -145.00$ ppm versus 85% H_3PO_4 in D_2O at $\delta = 0$ ppm. UV-Vis spectra were acquired using a Shimadzu UV-1900 spectrophotometer (Shimadzu, Kyoto, Japan) fitted with a temperature-controlled circulating water bath. Analytical HPLC was carried out using an Ultra Aqueous C18 column, 100 Å, 5 µm, 250 mm × 4.6 mm (Restek, Bellefonte, PA) using a 5–95% H_2O/MeCN method (15 min) at a flow rate of 1.0 mL/min. Elemental analyses (C, H, N) were carried out by Atlantic microlab Inc. (Norcross, GA). Inductively coupled plasma optical emission spectroscopy (ICP-OES) was performed using a PerkinElmer Avio 220 Max system. Standardized solutions of (0–2000 µg L^{-1}) of ruthenium, prepared from a standardized ICP mass spectrometry solution of Ru (1001 ± 4 mg L^{-1} in 10% HCl, Agilent Technologies, Santa Clara,

CA) were used to generate a calibration curve. The concentrations of all stock solutions of Ru compounds used in analytical experiments were verified by ICP-OES. Statistical analysis and curve fitting were performed using MagicPlot version 3.0.1 for Windows x64.

Synthesis of $[Ru(bpy)_2(GYY4137)][PF_6]$ (1)

$[Ru(bpy)_2Cl_2]$ (200 mg, 1 eq., 0.412 mmol) was dissolved in 20 mL of MeOH. $AgNO_3$ (140 mg, 2 eq., 0.825 mmol) was added, and the resulting solution was heated at reflux in the dark for 1 h. The resulting suspension was then filtered through a pad of celite to remove the insoluble AgCl byproducts. To the filtrate, GYY4137 (171 mg, 1.1 eq., 0.454 mmol) was added, and this solution was allowed to stir for 1 h at room temperature. The MeOH was removed under reduced pressure at ambient temperature, and $NaPF_6$ (693 mg, 10 eq., 4.13 mmol) in 2 mL of MeOH was added to the remaining residue. After storing this mixture at 4 °C overnight, a deep red solid formed, and it was collected by filtration and washed sequentially with water (5 mL), MeOH (1 mL, 4 °C), and diethyl ether (5 mL). This compound was further purified by allowing the vapor diffusion of diethyl ether into a dichloromethane solution. Crystals were collected and washed with 1 mL 1:1 dichloromethane/diethyl ether solution (233 mg, 66.6 %). ^{1}H NMR (500 MHz, CD_3CN) δ 10.19 (dd, J = 5.7, 1.5 Hz, 1H), 9.15 (dd, J = 5.7, 1.5 Hz, 1H), 8.47 (d, J = 8.1 Hz, 1H), 8.34 (d, *J* = 8.1 Hz, 2H), 8.28 (d, *J* = 8.1 Hz, 1H), 8.11 (td, *J* = 7.9, 1.5 Hz, 1H), 7.88–7.80 (m, 2H), 7.80–7.73 (m, 3H), 7.66 (d, *J* = 5.9 Hz, 1H), 7.61–7.54 (m, 2H), 7.14 (ddd, *J* = 7.3, 5.7, 1.3 Hz, 1H), 7.09 (ddd, *J* = 7.3, 5.8, 1.3 Hz, 1H), 6.99 (ddd, *J* = 7.3, 5.7, 1.4 Hz, 1H), 6.94–6.90 (m, 2H), 3.87 (s, 3H), 3.50 (m, 4H), 2.93 (m, 2H), 2.80 (m, 2H). ^{13}C{^{1}H} NMR (126 MHz, CD_3CN) δ 162.9, 162.9, 159.0, 158.9, 158.2, 158.0, 154.0, 153.7, 152.3, 151.9, 135.7, 135.6, 135.5, 135.0, 133.3, 133.2, 127.6, 126.8, 126.5, 125.7, 125.2, 123.2, 123.2, 122.9, 122.9, 117.3, 113.7, 113.6, 66.3, 66.3, 44.9, 44.9. ^{31}P{^{1}H}

NMR (202 MHz, CD_3CN) δ 103.06, –145.00 (sept, J = 708.40 Hz). HPLC: t_R = 8.68 min. IR (ATR, cm^{-1}): 757 (s), 834 (vs), 950 (s), 1108 (s), 1257 (s), 1300 (w), 1418 (s), 1447 (w), 1469 (s), 1595 (s), 2832 (w), 3666 (w). Anal Calcd for $[C_{31}H_{31}N_5O_2PRuS_2](PF_6)$: C, 43.97; H, 3.69; N, 8.27. Found: C, 43.42; H, 3.65; N, 8.07. ESI-MS calc for $[C_{31}H_{31}N_5O_2PRuS_2]^+$: 702.1. Found: 701.9 $[M]^+$

Synthesis of $[Ru(biq)_2(GYY4137)][PF_6]$ (2)

Compound **2** was prepared with an identical procedure for that of **1**, using $[Ru(biq)_2Cl_2]$ (310 mg, 1 eq., 0.452 mmol), $AgNO_3$ (153 mg, 2 eq., 0.905 mmol), GYY4137 (204 mg, 1.2 eq., 0.543 mmol), and $NaPF_6$ (761 mg, 10 eq., 4.53 mmol). Compound **2** was isolated as a deep blue solid and was further purified with vapor diffusion of diethyl ether into a chloroform solution (268 mg, 56.5 %). ^1H NMR (500 MHz, CD_3CN) δ 8.81 (d, J = 8.8 Hz, 1H), 8.73 (d, J = 8.9 Hz, 1H), 8.66 (d, J = 8.8 Hz, 1H), 8.64 (d, J = 8.9 Hz, 1H), 8.61–8.55 (m, 3H), 8.36 (d, J = 8.8 Hz, 1H), 8.05 (dd, J = 8.2, 1.4 Hz, 1H), 7.98 (dd, J = 8.2, 1.4 Hz, 1H), 7.93 (d, J = 8.1 Hz, 1H), 7.67–7.61 (m, 2H), 7.57 (ddd, J = 8.1, 7.1, 1.3 Hz, 1H), 7.42 (d, J = 8.8 Hz, 1H), 7.38 (ddd, J = 8.0, 6.9, 1.1 Hz, 1H), 7.33–7.21 (m, 3H), 7.08 (d, J = 8.8 Hz, 1H), 6.97–6.90 (m, 1H), 6.88 (ddd, J = 8.7, 6.8, 1.4 Hz, 1H), 6.78–6.66 (m, 4H), 6.40 (dd, J = 8.8, 2.8 Hz, 2H), 3.75 (s, 3H), 2.85 (s, 2H), 1.82 (m, 2H), 1.73 (m, , 2H). $^{13}C\{^1H\}$NMR (126 MHz, CD_3CN) δ 163.6, 163.4, 163.3, 162.9, 162.9, 152.9, 152.8, 151.3, 151.1, 138.2, 138.1, 137.5, 137.4, 133.0, 132.9, 132.0, 131.7, 131.6, 130.7, 129.9, 129.8, 129.8, 129.6, 129.4, 129.3, 129.2, 129.2, 129.1, 129.0, 128.9, 128.9, 128.7, 126.9, 126.7, 124.1, 123.2, 122.0, 121.9, 121.4, 120.9, 118.3, 114.4, 114.3, 66.7, 66.6, 56.1, 44.9. $^{31}P\{^1H\}$ NMR (202 MHz, CD_3CN) δ 92.14, –145.00 (sept, J = 708.40 Hz). HPLC: t_R = 10.35 min. IR (ATR, cm^{-1}): 748 (w), 812 (s), 847 (m), 951 (m), 1024 (m), 1109 (m), 1141 (m), 1251 (w), 1454 (w), 1507 (m), 1557 (w), 1592

(w), 2845 (w), 3066 (w). Anal Calcd for $[C_{47}H_{39}N_5O_2PRuS_2](PF_6)$: C, 53.92; H, 3.75; N, 6.69. Found: C, 53.96; H, 3.75; N, 6.63. ESI-MS calc for $[C_{47}H_{39}N_5O_2PRuS_2]^+$: 902.1. Found: 901.8 $[M]^+$

Synthesis of $[Ru(dmobpy)_2(GYY4137)][PF_6]$ (3)

Compound **3** was prepared with an identical procedure for that of **1**, using $[Ru(dmobpy)_2Cl_2]$ (150 mg, 1 eq., 0.248 mmol), $AgNO_3$ (84 mg, 2 eq., 0.496 mmol), GYY4137 (102 mg, 1.1 eq., 0.272 mmol), and $NaPF_6$ (417 mg, 10 eq., 2.48 mmol). This compound was purified by eluting it through a pad of 20% deactivated alumina (1 × 4 cm) in a solution of 33% toluene in acetone (R_f = 0.81). This compound was isolated as the leading red band and dried under reduced pressure to afford a purplish-red powder (78 mg, 32.5 %). ^{1}H NMR (500 MHz, CD_3CN) δ 9.91 (d, *J* = 6.5 Hz, 1H), 8.85 (d, *J* = 6.5 Hz, 1H), 8.00 (d, *J* = 2.8 Hz, 1H), 7.87 (t, *J* = 2.9 Hz, 2H), 7.81 (d, *J* = 2.8 Hz, 1H), 7.61 (m, 2H), 7.53 (d, *J* = 6.5 Hz, 1H), 7.45 (d, *J* = 6.6 Hz, 1H), 7.39 (dd, *J* = 6.5, 2.7 Hz, 1H), 6.93 (m, 2H), 6.74 (dd, *J* = 6.5, 2.7 Hz, 1H), 6.69 (dd, *J* = 6.6, 2.7 Hz, 1H), 6.55 (dd, *J* = 6.5, 2.7 Hz, 1H), 4.11 (s, 3H), 3.97 (s, 3H), 3.90 (s, 3H), 3.89 (s, 3H), 3.87 (s, 3H), 3.51 (m, 4H), 2.95 (m, 2H), 2.79 (m, 2H). ^{13}C{^{1}H} NMR (126 MHz, CD_3CN) δ 165.8, 165.7, 165.6, 165.3, 162.7, 162.7, 160.1, 160.0, 159.4, 159.2, 154.5, 154.3, 152.7, 152.3, 133.4, 133.3, 128.1, 127.3, 117.3, 113.6, 113.5, 113.0, 112.4, 112.4, 111.4, 109.9, 109.8, 109.8, 109.5, 66.4, 66.3, 56.4, 56.2, 56.2, 55.4, 44.8, 44.8. ^{31}P{^{1}H} NMR (202 MHz, CD_3CN) δ 103.06, –145.00 (sept, *J* = 708.40 Hz). HPLC: t_R = 9.78 min. IR (ATR, cm^{-1}): 821 (m), 835 (vs), 964 (s), 1002 (s), 1033 (s), 1104 (s), 1218 (s), 1256 (s), 1301 (s), 1326 (m), 1422 (m), 1486 (m), 1550 (s), 1613 (m), 1696 (m), 2857 (w), 2914 (w). Anal Calcd for $[C_{35}H_{39}N_5O_6PRuS_2](PF_6)\cdot$Acetone: C, 44.53; H, 4.43; N, 6.83. Found: C, 44.75; H, 4.55; N, 6.78. ESI-MS calc for $[C_{35}H_{39}N_5O_6PRuS_2]^+$: 822.1. Found: 821.7 $[M]^+$

Synthesis of $[Ru(dmtbpy)_2(GYY4137)][PF_6]$ (4)

Compound **4** was prepared analogously to **1**. $[Ru(dtbpy)_2Cl_2]$ (300 mg, 1 eq., 0.423 mmol) was used with $AgNO_3$ (72 mg, 2 eq., 0.619 mmol) and GYY4137 (128 mg, 1.1 eq., 0.340 mmol). A $NaPF_6$ (710 mg, 10 eq., 4.23 mmol) solution was added to obtain the product as a dark red solid. This compound was purified using vapor diffusion of hexanes into dichloromethane (311 mg, 68.6 %). ^{1}H NMR (500 MHz, CD_3CN) δ 10.06 (d, *J* = 6.0 Hz, 1H), 9.02 (d, *J* = 6.1 Hz, 1H), 8.50 (d, *J* = 2.1 Hz, 1H), 8.36 (d, *J* = 2.1 Hz, 1H), 8.33 (d, *J* = 2.1 Hz, 1H), 8.29 (d, *J* = 2.1 Hz, 1H), 7.86 (dd, *J* = 6.1, 2.1 Hz, 1H), 7.63–7.57 (m, 4H), 7.18 (dd, *J* = 6.2, 2.1 Hz, 1H), 7.13 (dd, *J* = 6.2, 2.1 Hz, 1H), 6.97–6.92 (m, 3H), 3.89 (s, 3H), 3.59–3.46 (m, 4H), 2.95 (m, 2H), 2.83 (m, 2H), 1.58 (s, 9H), 1.45 (s, 9H), 1.35 (s, 9H), 1.35 (s, 9H). ^{13}C{^{1}H}NMR (126 MHz, CD_3CN) δ 162.8, 162.7, 160.1, 160.1, 159.4, 158.9, 158.8, 157.9, 157.7, 153.3, 153.0, 151.6, 151.1, 150.7, 133.5, 133.4, 127.6, 126.8, 124.6, 123.7, 122.9, 122.2, 121.4, 120.4, 120.4, 120.0, 119.9, 113.7, 113.5, 66.4, 66.3, 55.3, 44.9, 44.9, 35.3, 35.2, 35.0, 34.9, 34.9, 29.8, 29.7, 29.5, 29.5, 29.4. ^{31}P{^{1}H} NMR (202 MHz, CD_3CN) δ 101.74, –145.00. HPLC: t_R = 14.01 min. IR (ATR, cm^{-1}): 662 (w), 695 (m), 829 (vs), 956 (m), 1104 (m), 1253 (m), 1415 (m), 1474 (m), 1557 (m), 2362 (w), 2963 (w). Anal Calcd for $[C_{47}H_{63}N_5O_2PRuS_2](PF_6)\cdot 1.2H_2O$: C, 51.66; H, 6.03; N, 6.44. Found: C, 51.34; H, 5.75; N, 6.29. ESI-MS calc for $[C_{47}H_{63}N_5O_2PRuS_2]^+$: 926.3 Found: 926.0 $[M]^+$

X-ray Crystallography

Single crystals of **1** and **3** were obtained by vapor diffusion of diethyl ether into dichloromethane solutions of the complexes. Crystals of compound **2** were afforded by the vapor diffusion of diethyl ether into a chloroform solution of the trifluoroacetate salt of this compound. Crystals of **4** were obtained by layering hexanes over a chloroform solution of the compound.

Low-temperature X-ray diffraction data for **2** and **3** were collected on a Rigaku XtaLAB Synergy diffractometer coupled to a Rigaku Hypix detector with either Mo Kα radiation (λ = 0.71073 Å) or Cu Kα radiation (λ = 1.54184 Å), from PhotonJet micro-focus X-ray sources at 100 K. The diffraction images were processed and scaled using the CrysAlisPro software (Rigaku Oxford Diffraction, The Woodlands TX). The structures were solved through intrinsic phasing using SHELXT[91] and refined against F^2 on all data by full matrix least squares with SHELXL[92] following established refinement strategies.[93] All nonhydrogen atoms were refined anisotropically. All hydrogen atoms bound to carbon were included in the model at geometrically calculated positions and refined using a riding model. Low-temperature X-ray diffraction data for **1** and **4** were collected on a Bruker Kappa Apex II diffractometer equipped with CCD detector and Mo fine focus sealed tube with TRIUMPH monochromator. This system is also equipped with Oxford Cryostream-Plus. Diffraction images were processed using the Bruker Apex software suite. The structure was solved using intrinsic phasing using SHELXT and refined against F^2 on all data by full-matrix least-squares with SHELXL following established strategies. All non-hydrogen atoms were refined anisotropically. Details of the data quality and a summary of the residual values of the refinements are listed in Table S1.

The CheckCIF analysis of the cif file of compound **1** gave rise to a B-level alert, noting significant discrepancies between F_{obs} and F_{calc} for 10 reflections. These outliers are most likely a consequence of the crystal quality, which was also apparent from the overall weak intensity of diffraction and lower resolution. Diethyl ether (Et_2O) was present within this crystal, and it resided on a special position, resulting in the 0.5 equivalents of Et_2O per unit formula. Within the crystal structure of the trifluoroacetate salt of compound **2**, a positionally disordered chloroform molecule

was present. This disorder was modeled using appropriate distance and thermal displacement restraints. Compound **4** crystallized with rotational and positional disorder within the *tert*-butyl and morpholine moieties. These disorders were modeled using appropriate distance and thermal displacement restraints, while allowing the occupancies of the disordered components to freely refine to a sum of unity.

UV-Vis Monitoring of Photoreaction

A custom-built UV-Vis setup employing a hybrid tungsten-halogen/deuterium light source (Ocean Optics HL2000-BAL), which is connected via a quartz optical fiber to a collimator (Ocean Optics), was used for these studies. The probe beam emerging from the collimator was focused and recollimated to approximately 1 mm in diameter using quartz lenses. A sample holder designed for 10×10 mm cells was placed in line with the beam, allowing optical access from all four sides. The beam was subsequently focused onto another fiber collimator, and a quartz fiber delivered the light to an Ocean Optics Flame XR spectrometer. A computer-controlled shutter (Thorlabs) was used to block the probe beam as needed. Spectra were collected between 280–1000 nm.

The 470 nm light was generated by a fiber-coupled light-emitting diode (LED) (Thorlabs), with output power controlled via computer-generated voltage signals using a Thorlabs LEDD1B power supply. The collimated LED output was directed perpendicularly through the sample relative to the probe beam. The LED output power was measured using a Newport 842PE power meter with an 818-UV detector head. The sample cell contents were stirred using a low-profile magnetic stirrer (Starna Spinette). Control voltages for both the LED light source and the probe shutter were generated using a National Instruments USB-6008 I/O module.

Data collection was managed by a custom-developed program written in National Instruments LabVIEW. The software enables the acquisition of time-resolved optical absorption data during LED irradiation, as well as monitoring of post-irradiation absorption kinetics.

Initially, the data were collected using the 470 nm pump source with acquisition of spectra at increments of 30 s for 63000 s. The data used in the computation of quantum yield was split under continuous irradiation. Initially, scans were collected every 2 s for 900 s and subsequently scans were taken every 900 s until a total irradiation time of 63900 s. The data was exported and a smoothing function was applied using a moving average method and 40 windowing points to minimize data noise in MagicPlot version 3.0.1.

HPLC Monitoring of Photoreaction

Solutions of 100 μM of the complexes were prepared in MeCN using stocks prepared in MeCN solution. A 20 mL quantity of these solutions was placed into a glass scintillation vial equipped with a magnetic stir bar. The scintillation vial was placed into the LED irradiation chamber (Figure 3 and Figures S35, SI) with the magnetic stirring plate on. Aliquots were removed at 0, 0.5, 1, 2, 3, 4, 5, 6, and 24 h and run on the LC-MS equipped with ESI-MS detection using a 15 min 5–95% MeCN/H_2O method. ESI-MS and photodiode array detector spectra (PDA) spectra were used to assign peaks as either intact complex, monodentate dechelation product, $[Ru(NN)_2(MeCN)_2]^{2+}$, and $[Ru(NN)(GYY4137)(MeCN)_2]^{+}$ photolysis photoproducts.

Quantum Yield Calculations

These calculations were performed using previously developed software adapted for the MATLAB computing platform.[69] The computational program determines photochemical quantum

yields, computes molar absorption profiles and molarity kinetics for the initial reactant (1) and two sequential products (2 and 3) based on the provided time-resolved UV-Vis absorption spectra and the photon flux spectrum of the light source (See photochemABC1_ml.m and OOS2einstein.m, see supporting information). The kinetics of a three-component photochemical reaction are described by a system of master rate equations (Eq. 1-4). We added a term $k_{-1}C_2$ to Eq.1 and Eq.2 to account for the thermal rechelation process. A MATLAB script iteratively solves the system of equations and compares solutions with the input experimental data to determine values of the photochemical reaction quantum yields Φ_i and molar absorption spectra $\varepsilon_i(\lambda)$, which provide the smallest value of the root mean square deviation (RSMD) (Eq. 5) between the experimentally determined UV-Vis absorption spectra and the photochemical model predictions (See abcomp.m, see supporting information). In Eq.5, indices *i* and *j* correspond to wavelength and time steps, respectively.

$$\frac{dC_1}{dt} = -k_{ph}^1 C_1 + k_{-1} C_2 \qquad \text{(Eq. 1)}$$

$$\frac{dC_2}{dt} = k_{ph}^1 C_1 - k_{ph}^2 C_2 - k_{-1} C_2 \qquad \text{(Eq.2)}$$

$$\frac{dC_3}{dt} = k_{ph}^2 C_2 \qquad \text{(Eq.3)}$$

$$k_{ph}^i = \Phi_i \int I_0(\lambda)\left(1 - 10^{-A_t(\lambda)}\right) \frac{\varepsilon_i(\lambda)}{\varepsilon_1(\lambda)C_1 + \varepsilon_2(\lambda)C_2 + \varepsilon_3(\lambda)C_3} d\lambda \qquad \text{(Eq.4)}$$

$$\Omega_A = \left[\sum_{i,j} \left((A_{\exp} - A)_{ij}\right)^2\right]^{1/2} \qquad \text{(Eq. 5)}$$

k_{ph}^i is the rate constant for the i^{th} step of the photochemical reaction. It is determined based on the light source photon flux spectrum and the optical absorption coefficient of the i^{th} reaction

component. Thermal rechelation of the second component competes with the photoinduced process, however its rate constant k_{-1} is about three orders of magnitude smaller than k_{ph}^{1} and has no statistically noticeable influence on the calculation results.

Using the UV-Vis setup described above, irradiation of samples was performed in two phases. Samples were prepared at 30 μM in HPLC-grade acetonitrile. In the first phase of the irradiation, scans were acquired every 2 s for 900 s. After this first phase, scans were acquired every 900 s until a total reaction time of 63900 s. The time step has been increased after 900 s of irradiation because it allowed for a decrease in the size of the resulting data file without decreasing the quality of the data due to the low rate of the second step of the photochemical reaction. Additionally, LED output power measurements were made for each replicate using a Newport 842PE power meter with an 818-UV detector head. This value, read out in units of mW, was used in combination with the spectrum of the irradiation source collected with an Ocean Optics Flame XR spectrometer to capture the spectral output of the LED in units of Einstein·s^{-1} dm^{-3} nm^{-1}.

To validate our method, this protocol was used to fit the photochemical aquation of $[Ru(bpy)_2(MeCN)_2]^{2+}$ to $[Ru(bpy)_2(H_2O)_2]^{2+}$ as previously described (see file photochemABC_ml.m, see supporting information).[69] The resulting values and Ω_A for the data fitting are presented in Figure S42, SI. The values of Φ_1 and Φ_2 (0.43 and 0.023) measured with our experimental setup are in good agreement with those reported in the literature, which found Φ_1 and Φ_2 to be 0.44 and 0.033.[70] The overall quantum yields, not accounting for a two-step reactions, were also studied by others and found to be 0.44 in 1 M H_2SO_4 and 0.22 in unbuffered water.[69,94,95]

Thermal Rechelation to Intact Complex

A 30 μM sample of the complex in MeCN was irradiated with a 470 nm LED for 150 s at 25 °C with stirring. This time was selected to ensure that the majority of the complex in solution existed as the monodentate intermediate. The reaction mixture was allowed to stir in the dark for another 4 h, with scans taken every 10 minutes as the absorbance of the intact complex MLCT band was monitored. The rate constant of the regrowth of this peak was determined from the inverse exponential fit of the recovery curve (Eq. 6). In the equation below, A is the absorbance of the solution at λ_{MLCT}, t is the time corresponding to the given absorbance, b is the initial absorbance of the solution at t = 0, the sum of C and b is the final absorbance of the solution, and *k* is the first-order rate constant for rechelation.

$$A = C(1 - e^{-kt}) + b \qquad \text{(Eq. 6)}$$

Computational Studies

DFT calculations were performed using Gaussian 16[73] and carried out using the PBE1PBE[74,96,97] hybrid functional. The LANL2DZ basis set and effective core potential[98] were used for ruthenium atoms, and the 6-31G(d,p)[75,76] basis set was adopted for the light elements (C, H, N, O, S, P). Geometry optimizations for the intact complex and photoproducts were performed in a self-consistent reaction field (SCRF) using an SMD model[77] to simulate the solvation of the compounds in acetonitrile. Starting geometries of the intact complexes were modeled after their crystal structures. Monodentate intermediates and the final photoproducts were modeled from the optimized geometries of the intact complexes by adjusting the coordination sphere accordingly to include one solvent ligand. The monodentate intermediates were optimized first in the gas phase.

The gas phase-optimized geometry was reoptimized using the SMD solvation model. After all geometry optimizations, frequency calculations were performed to ensure that all structures had converged to local minima on their respective potential energy surfaces, as verified by the absence of imaginary frequencies. The cartesian coordinates of SCM-optimized structures are provided in the Supporting Information.

The DFT calculations were used to determine Gibbs free energies for the species shown in Eqs. S4–S7, enabling standard free energy differences (ΔG°) for these reactions to be calculated. Eqs. S4–S5 represent the reaction pathway that involves dissociation of GYY4137, whereas Eqs. S6–S7 are for the pathway in which the diimine ligand departs.

$[Ru(NN)_2(GYY4137)]^+ + MeCN \rightarrow [Ru(NN)_2(\kappa^1\text{-}GYY4137)(MeCN)]^+$ (Eq. 7)

$[Ru(NN)_2(\kappa^1\text{-}GYY4137)(MeCN)]^+ + MeCN \rightarrow [Ru(NN)_2(MeCN)_2]^{2+} + GYY4137$ (Eq. 8)

$[Ru(NN)_2(GYY4137)]^+ + MeCN \rightarrow [Ru(NN)(\kappa^1\text{-}NN)(GYY4137)(MeCN)]^+$ (Eq. 9)

$[Ru(NN)(\kappa^1\text{-}NN)(GYY4137)]^+ + MeCN \rightarrow [Ru(NN)(GYY4137)(MeCN)_2]^+$ (Eq. 10)

Default settings in Gaussian16 yield free energies under standard state conditions in the gas phase (1 atm, 298 K). To adjust these values for standard state solution conditions (1 M concentration for solute or pure liquid state for solvent), a correction to the gas-phase free energy terms was applied. For solutes, the correction factor in moving from 1 atm (or 1/24.5 M) follows the following expression:

$$RTln\left(\frac{1\,M}{1\,atm}\right) = RTln(24.5) = 7.9\,kJ \bullet mol^{-1}$$

For MeCN, a pure liquid, the free energy was adjusted to account for the energy change in moving from the concentration of 1 atm MeCN to that of pure liquid MeCN (19.5 M):

$$RTln\left(\frac{19.15\,M}{1\,atm}\right)=RTln(469)=15.2\,kJ\bullet mol^{-1}$$

Acknowledgements

This research was supported by Cornell University, the University of California Santa Barbara, and the National Science Foundation (NSF) of the United States of America under award number CHE-2203369. This work made use of the University of California Santa Barbara NMR facility, which is supported in part by NSF Major Research Instrumentation award MRI-1920299.

Conflicts of Interest

The authors declare no conflict of interest.

Associated Content

Supporting Information

The Supporting Information is available free of charge at

- Supplementary data for chemical synthesis, UV-Vis irradiation, thermal rechelation, NMR spectroscopic data, X-ray crystallographic tables, and calculated energy of optimized structures (PDF)
- XYZ coordinates of computed structures (ZIP)
- Crystallographic data including .cif files and IUCr CheckCIF for **1**, **2**, **3**, and **4**. (ZIP)
- MATLAB scripts for quantum yield calculations (ZIP)

Accession Codes

CCDC 2528694−2528697 contain the supplementary crystallographic data for this paper. These data can be obtained free of charge via www.ccdc.cam.ac.uk/data_request/cif, or by emailing data_request@ccdc.cam.ac.uk, or by contacting The Cambridge Crystallographic Data Centre, 12 Union Road, Cambridge CB2 1EZ, UK; fax: +44 1223 336033.

Author Information

Corresponding Author

Justin J. Wilson – *Department of Chemistry and Biochemistry, University of California, Santa Barbara, California 93106, United States; Department of Chemistry and Chemical Biology, Cornell University, Ithaca, New York 14853, United States;* orcid.org/0000-0002-4086-7982; Email: justinjwilson@ucsb.edu

Authors

Piyusha S. Lotlikar – *Department of Chemistry and Chemical Biology, Cornell University, Ithaca, New York 14853, United States; Department of Chemistry and Biochemistry, University of California, Santa Barbara, California 93106, United States;* orcid.org/0000-0002-0458-9655

Valerie Chang – *Department of Chemistry and Chemical Biology, Cornell University, Ithaca, New York 14850, United States; orcid.org/0000-0002-3156-3995*

Alexander A. Mikhailovsky – *Department of Chemistry and Biochemistry, University of California, Santa Barbara, California 93106, United States*

Joshua J. Woods – *Department of Chemistry and Chemical Biology, Cornell University, Ithaca, New York 14853, United States; Robert F. Smith School of Engineering, Cornell University, Ithaca, New York 14853, United States; Present Address: Chemical Sciences Division, Lawrence Berkeley National Laboratory, Berkeley, California 94720, United States;* orcid.org/0000-0002-6213-4093

Nicholas P. Bigham – *Department of Chemistry and Chemical Biology, Cornell University, Ithaca, New York 14853, United States;* orcid.org/0000-0001-9188-145

References

(1) Abe, K.; Kimura, H. The Possible Role of Hydrogen Sulfide as an Endogenous Neuromodulator. *J. Neurosci.* **1996**, *16*, 1066–1071. https://doi.org/10.1523/JNEUROSCI.16-03-01066.1996.

(2) Blackstone, E.; Morrison, M.; Roth, M. B. H_2S Induces a Suspended Animation-Like State in Mice. *Science* **2005**, *308*, 518. https://doi.org/10.1126/science.1108581.

(3) Wang, R. Two's Company, Three's a Crowd: Can H_2S Be the Third Endogenous Gaseous Transmitter? *FASEB J.* **2002**, *16*, 1792–1798. https://doi.org/10.1096/fj.02-0211hyp.

(4) Filipovic, M. R.; Zivanovic, J.; Alvarez, B.; Banerjee, R. Chemical Biology of H_2S Signaling through Persulfidation. *Chem. Rev.* **2017**, *118*, 1253–1337. https://doi.org/10.1021/acs.chemrev.7b00205.

(5) Szabó, C. Hydrogen Sulphide and Its Therapeutic Potential. *Nat. Rev. Drug Discov.* **2007**, *6*, 917–935. https://doi.org/10.1038/nrd2425.

(6) Tabassum, R.; Jeong, N. Y. Potential for Therapeutic Use of Hydrogen Sulfide in Oxidative Stress-Induced Neurodegenerative Diseases. *Int. J. Med. Sci.* **2019**, *16*, 1386–1396. https://doi.org/10.7150/ijms.36516.

(7) Zhang, X.; Bian, J.-S. Hydrogen Sulfide: A Neuromodulator and Neuroprotectant in the Central Nervous System. *ACS Chem. Neurosci.* **2014**, *5*, 876–883. https://doi.org/10.1021/cn500185g.

(8) Polhemus, D. J.; Lefer, D. J. Emergence of Hydrogen Sulfide as an Endogenous Gaseous Signaling Molecule in Cardiovascular Disease. *Circ. Res.* **2014**, *114*, 730–737. https://doi.org/10.1161/CIRCRESAHA.114.300505.

(9) Sun, H.-J.; Wu, Z.-Y.; Nie, X.-W.; Bian, J.-S. Role of Endothelial Dysfunction in Cardiovascular Diseases: The Link Between Inflammation and Hydrogen Sulfide. *Front. Pharmacol.* **2020**, *10*, 1568. https://doi.org/10.3389/fphar.2019.01568.

(10) Chen, F. E.; Mandel, R. M.; Woods, J. J.; Lee, J.-H.; Kim, J.; Hsu, J. H.; Jos´, J.; Fuentes-Rivera, J. J.; Wilson, J. J.; Milner, P. J. Biocompatible Metal-Organic Frameworks for the Storage and Therapeutic Delivery of Hydrogen Sulfide. *Chem. Sci.* **2021**, *12*, 7848–7857. https://doi.org/10.1039/d1sc00691f.

(11) Mandel, R. M.; Lotlikar, P. S.; Runčevski, T.; Lee, J.-H.; Woods, J. J.; Pitt, T. A.; Wilson, J. J.; Milner, P. J. Transdermal Hydrogen Sulfide Delivery Enabled by Open-Metal-Site Metal–Organic Frameworks. *J. Am. Chem. Soc.* **2024**, *146*, 18927–18937. https://doi.org/10.1021/jacs.4c00674.

(12) Allan, P. K.; Wheatley, P. S.; Aldous, D.; Mohideen, M. I.; Tang, C.; Hriljac, J. A.; Megson, I. L.; Chapman, K. W.; De Weireld, G.; Vaesen, S.; Morris, R. E. Metal–Organic Frameworks for the Storage and Delivery of Biologically Active Hydrogen Sulfide. *Dalton Trans.* **2012**, *41*, 4060–4066. https://doi.org/10.1039/c2dt12069k.
(13) Pinto, R. V.; Carvalho, S.; Antunes, F.; Pires, J.; Pinto, M. L. Development of Polycaprolactone–Zeolite Nanoporous Composite Films for Topical Therapeutic Release of Different Gasotransmitters. *ACS Appl. Nano Mater.* **2022**, *5*, 9230–9240. https://doi.org/10.1021/acsanm.2c01591.
(14) Fernandes, A. C.; Pinto, R.; Carvalho, S.; Mafra, L.; Rocha, J.; Pinto, M.; Antunes, F.; Pires, J. Storage and Delivery of H₂S by Microporous and Mesoporous Materials. *Microporous Mesoporous Mater.* **2021**, *320*, 111093. https://doi.org/10.1016/j.micromeso.2021.111093.
(15) Liao, L.-G.; Ke, D.; Li, G.-C.; Zhang, S.; Li, B.-J. Cyclodextrin Metal-Organic Framework as a Broad-Spectrum Potential Delivery Vehicle for the Gasotransmitters. *Molecules* **2023**, *28*, 852. https://doi.org/10.3390/molecules28020852.
(16) Powell, C. R.; Dillon, K. M.; Matson, J. B. A Review of Hydrogen Sulfide (H_2S) Donors: Chemistry and Potential Therapeutic Applications. *Biochem. Pharmacol.* **2018**, *149*, 110–123. https://doi.org/10.1016/j.bcp.2017.11.014.
(17) Levinn, C. M.; Cerda, M. M.; Pluth, M. D. Activatable Small-Molecule Hydrogen Sulfide Donors. *Antioxid. Redox Signal.* **2020**, *32*, 79–159. https://doi.org/10.1089/ars.2019.7841.
(18) Szabo, C.; Papapetropoulos, A. International Union of Basic and Clinical Pharmacology. CII: Pharmacological Modulation of H_2S Levels: H_2S Donors and H_2S Biosynthesis Inhibitors. *Pharmacol. Rev.* **2017**, *69*, 497–564. https://doi.org/10.1124/pr.117.014050.
(19) Li, L.; Whiteman, M.; Guan, Y. Y.; Neo, K. L.; Cheng, Y.; Lee, S. W.; Zhao, Y.; Baskar, R.; Tan, C. H.; Moore, P. K. Characterization of a Novel, Water-Soluble Hydrogen Sulfide-Releasing Molecule (GYY4137): New Insights into the Biology of Hydrogen Sulfide. *Circulation* **2008**, *117*, 2351–2360. https://doi.org/10.1161/CIRCULATIONAHA.107.753467.
(20) Kang, J.; Li, Z.; Organ, C. L.; Park, C. M.; Yang, C. T.; Pacheco, A.; Wang, D.; Lefer, D. J.; Xian, M. pH-Controlled Hydrogen Sulfide Release for Myocardial Ischemia-Reperfusion Injury. *J. Am. Chem. Soc.* **2016**, *138*, 6336–6339. https://doi.org/10.1021/jacs.6b01373.
(21) Jiao, Y.; Ye, H.; Huang, H.; Yi, L.; Sun, L. Thiobenzophenones: Tunable Hydrolysis-Based Donors for Intracellular H2S Delivery. *New J. Chem.* **2022**, *46*, 7859–7863. https://doi.org/10.1039/D2NJ01152B.
(22) Gilbert, A. K.; Zhao, Y.; Otteson, C. E.; Pluth, M. D. Development of Acid-Mediated H_2S/COS Donors That Respond to a Specific pH Window. *J. Org. Chem.* **2019**, *84*, 14469–14475. https://doi.org/10.1021/acs.joc.9b01873.
(23) Hammers, M. D.; Singh, L.; Montoya, L. A.; Moghaddam, A. D.; Pluth, M. D. Synthesis of Amino-ADT Provides Access to Hydrolytically Stable Amide-Coupled Hydrogen Sulfide Releasing Drug Targets. *Synlett* **2016**, *27*, 1349–1353. https://doi.org/10.1055/s-0035-1560603.
(24) Woods, J. J.; Cao, J.; Lippert, A. R.; Wilson, J. J. Characterization and Biological Activity of a Hydrogen Sulfide-Releasing Red Light-Activated Ruthenium(II) Complex. *J. Am. Chem. Soc.* **2018**, *140*, 12383–12387. https://doi.org/10.1021/jacs.8b08695.
(25) Zhao, Y.; Bolton, S. G.; Pluth, M. D. Light-Activated COS/H_2S Donation from Photocaged Thiocarbamates. *Org. Lett.* **2017**, *19*, 2278–2281. https://doi.org/10.1021/acs.orglett.7b00808.
(26) Venkatesh, Y.; Das, J.; Chaudhuri, A.; Karmakar, A.; Maiti, T. K.; Singh, N. D. P. Light Triggered Uncaging of Hydrogen Sulfide (H_2S) with Real-Time Monitoring. *Chem. Commun.* **2018**, *54*, 3106–3109. https://doi.org/10.1039/C8CC01172A.

(27) Bera, M.; Maji, S.; Paul, A.; Ray, S.; Maiti, T. K.; Singh, N. D. P. A Water Soluble Light Activated Hydrogen Sulfide Donor Induced by an Excited State Meta Effect. *Org. Biomol. Chem.* **2019**, *17*, 9059–9064. https://doi.org/10.1039/C9OB01502G.
(28) Yuan, F.; Guo, A.; Wang, L.; Ning, L.; Guo, Y.; Zhang, J. Tunable Light-Activated Platform for Controlled Hydrogen Sulfide Release with Tracking. *Angew. Chem. Int. Ed.* **2025**, *64*, e202501685. https://doi.org/10.1002/anie.202501685.
(29) Hanc, K.; Janeková, H.; Štacko, P. Concurrent Subcellular Delivery of Hydrogen Sulfide and a Payload with Near-Infrared Light. *JACS Au* **2024**, *4*, 2687–2694. https://doi.org/10.1021/jacsau.4c00445.
(30) Chaudhuri, A.; Singha, T.; Jena, B. C.; Shee, M.; Datta, P. K.; Mandal, M.; Singh, N. D. P. A Two-Photon Responsive Hydroxyphenylquinazolinone (HPQ)-Based Fluorescent Organic Nanoprodrug for H_2S Release against Oxidative Stress. *Chem. Commun.* **2023**, *59*, 1177–1180. https://doi.org/10.1039/D2CC05768A.
(31) Yuan, F.; He, X.; Lu, Y.; Ning, L.; Zhao, X.; Zhang, S.; Guan, F.; Guo, Y.; Zhang, J. Photoactivated Hydrogen Sulfide Donor with a Near-Infrared Fluorescence Report System for Accelerated Chronic Wound Healing. *Anal. Chem.* **2023**, *95*, 6931–6939. https://doi.org/10.1021/acs.analchem.3c00230.
(32) Zhao, Y.; Steiger, A. K.; Pluth, M. D. Cysteine-Activated Hydrogen Sulfide (H_2S) Delivery through Caged Carbonyl Sulfide (COS) Donor Motifs. *Chem. Commun.* **2018**, *54*, 4951–4954. https://doi.org/10.1039/C8CC02428F.
(33) Zhao, Y.; Steiger, A. K.; Pluth, M. D. Cyclic Sulfenyl Thiocarbamates Release Carbonyl Sulfide and Hydrogen Sulfide Independently in Thiol-Promoted Pathways. *J. Am. Chem. Soc.* **2019**, *141*, 13610–13618. https://doi.org/10.1021/jacs.9b06319.
(34) Garcia, A. C.; Zakharov, L. N.; Pluth, M. D. Supramolecular Activation of S_8 by Cucurbiturils in Water and Mechanism of Reduction to H_2S by Thiols: Insights into Biological Sulfane Sulfur Trafficking. *J. Am. Chem. Soc.* **2022**, *144*, 15324–15332. https://doi.org/10.1021/jacs.2c06332.
(35) Grace, J. P.; Bowden, N. B. Synthesis and Hydrogen Sulfide Releasing Properties of Diaminodisulfides and Dialkoxydisulfides. *ACS Omega* **2021**, *6*, 17741–17747. https://doi.org/10.1021/acsomega.1c02585.
(36) Hamsath, A.; Wang, Y.; Yang, C.; Xu, S.; Cañedo, D.; Chen, W.; Xian, M. Acyl Selenyl Sulfides as the Precursors for Reactive Sulfur Species (Hydrogen Sulfide, Polysulfide, and Selenyl Sulfide). *Org. Lett.* **2019**, *21*, 5685–5688. https://doi.org/10.1021/acs.orglett.9b02021.
(37) Ercole, F.; Whittaker, M. R.; Halls, M. L.; Boyd, B. J.; Davis, T. P.; Quinn, J. F. Garlic-Inspired Trisulfide Linkers for Thiol-Stimulated H_2S Release. *Chem. Commun.* **2017**, *53*, 8030–8033. https://doi.org/10.1039/C7CC03820H.
(38) Zhang, N.; Fu, T.; Li, T.; Zhong, P.; Li, L.; Peng, M.; Li, Z.; Zhang, L.; Wang, H.; Hu, P.; Lu, Y.; Yao, M. A Superoxide Anion Responsive and Self-Reporting Fluorescent H_2S Donor for the Treatment of Diabetic Wound. *Free Radic. Biol. Med.* **2025**, *231*, 109–119. https://doi.org/10.1016/j.freeradbiomed.2025.02.026.
(39) Powell, C. R.; Dillon, K. M.; Wang, Y.; Carrazzone, R. J.; Matson, J. B. A Persulfide Donor Responsive to Reactive Oxygen Species: Insights into Reactivity and Therapeutic Potential. *Angew. Chem. Int. Ed.* **2018**, *57*, 6324–6328. https://doi.org/10.1002/anie.201803087.
(40) Lu, H.; Zeng, H.; Wei, W.; Chen, Y.; Zhou, Z.; Ning, X.; Hu, P. A Fluorogenic ROS-Triggered Hydrogen Sulfide Donor for Alleviating Cerebral Ischemia-Reperfusion Injury. *Theranostics* **2024**, *14*, 7589–7603. https://doi.org/10.7150/thno.100930.
(41) Zhao, Y.; Pluth, M. D. Hydrogen Sulfide Donors Activated by Reactive Oxygen Species. *Angew. Chem.* **2016**, *128*, 14858–14862. https://doi.org/10.1002/ange.201608052.
(42) Hu, Q.; Zhu, C.; Hankins, R. A.; Murmello, A. R.; Marrs, G. S.; Lukesh, J. C. III. An ROS-Responsive Donor That Self-Reports Its H_2S Delivery by Forming a Benzoxazole-Based Fluorophore. *J. Am. Chem. Soc.* **2023**, *145*, 25486–25494. https://doi.org/10.1021/jacs.3c10446.

(43) Zhu, C.; Suarez, S. I.; Lukesh, J. C. Illuminating and Alleviating Cellular Oxidative Stress with an ROS-Activated, H_2S-Donating Theranostic. *Tetrahedron Lett.* **2021**, *69*, 152944. https://doi.org/10.1016/j.tetlet.2021.152944.
(44) Li, L.; Zhang, Z. A Fluorogenic H_2S Donor Activated by Reactive Oxygen Species for Real-Time Monitoring in Cells and *in Vivo*. *Spectrochim. Acta. A. Mol. Biomol. Spectrosc.* **2022**, *264*, 120243. https://doi.org/10.1016/j.saa.2021.120243.
(45) Zhang, N.; Hu, P.; Wang, Y.; Tang, Q.; Zheng, Q.; Wang, Z.; He, Y. A Reactive Oxygen Species (ROS) Activated Hydrogen Sulfide (H_2S) Donor with Self-Reporting Fluorescence. *ACS Sens.* **2020**, *5* (2), 319–326. https://doi.org/10.1021/acssensors.9b01093.
(46) Liu, J.; Zhao, M.; Zhao, F.; Song, X.; Ye, Y. $ONOO^-$Triggered Fluorescence H_2S Donor for Mitigating Drug-Induced Liver Injury. *Sens. Actuators B Chem.* **2023**, *378*, 133131. https://doi.org/10.1016/j.snb.2022.133131.
(47) Yao, M.; Lu, Y.; Shi, L.; Huang, Y.; Zhang, Q.; Tan, J.; Hu, P.; Zhang, J.; Luo, G.; Zhang, N. A ROS-Responsive, Self-Immolative and Self-Reporting Hydrogen Sulfide Donor with Multiple Biological Activities for the Treatment of Myocardial Infarction. *Bioact. Mater.* **2022**, *9*, 168–182. https://doi.org/10.1016/j.bioactmat.2021.07.011.
(48) Shyaka, C.; Xian, M.; Park, C.-M. Esterase-Sensitive Trithiane-Based Hydrogen Sulfide Donors. *Org. Biomol. Chem.* **2019**, *17*, 9999–10003. https://doi.org/10.1039/C9OB02273B.
(49) Jin, H.; Ma, J.; Xu, B.; Xu, S.; Hu, T.; Jin, X.; Wang, J.; Wang, G.; Zhen, L. Thio-ProTide Strategy: A Novel H_2S Donor–Drug Conjugate (DDC) Alleviates Hepatic Injury *via* Innate Lysosomal Targeting. *Acta Pharm. Sin. B* **2024**, *14*, 5341–5356. https://doi.org/10.1016/j.apsb.2024.10.017.
(50) Mechanism of H_2S Formation from the Metabolism of Anetholedithiolethione and Anetholedithiolone by Rat Liver Microsomes. *Drug Metab. Dispos.* **2019**, *47*, 1061–1065. https://doi.org/10.1124/dmd.119.087205.
(51) Steiger, A. K.; Marcatti, M.; Szabo, C.; Szczesny, B.; Pluth, M. D. Inhibition of Mitochondrial Bioenergetics by Esterase-Triggered COS/H_2S Donors. *ACS Chem. Biol.* **2017**, *12*, 2117–2123. https://doi.org/10.1021/acschembio.7b00279.
(52) Chen, J.; Bai, X.; Peng, W.; Liu, J.; Jia, Z.; Cheng, M.; Li, J.; Guo, W.; Zheng, Y. A Thiocoumarin Based Self-Reporting Sulfide Prodrug Strategy with a Favorable Safety Profile. *Eur. J. Med. Chem.* **2025**, *289*, 117426. https://doi.org/10.1016/j.ejmech.2025.117426.
(53) Zhu, Y.; Archer, W. R.; Morales, K. F.; Schulz, M. D.; Wang, Y.; Matson, J. B. Enzyme-Triggered Chemodynamic Therapy via a Peptide-H_2S Donor Conjugate with Complexed Fe^{2+}. *Angew. Chem. Int. Ed.* **2023**, *62*, e202302303. https://doi.org/10.1002/anie.202302303.
(54) Chauhan, P.; Bora, P.; Ravikumar, G.; Jos, S.; Chakrapani, H. Esterase Activated Carbonyl Sulfide/Hydrogen Sulfide (H_2S) Donors. *Org. Lett.* **2017**, *19*, 62–65. https://doi.org/10.1021/acs.orglett.6b03336.
(55) Zheng, Y.; Yu, B.; Ji, K.; Pan, Z.; Chittavong, V.; Wang, B. Esterase-Sensitive Prodrugs with Tunable Release Rates and Direct Generation of Hydrogen Sulfide. *Angew. Chem. Int. Ed.* **2016**, *128*, 4590–4594. https://doi.org/10.1002/ange.201511244.
(56) Woods, J. J.; Wilson, J. J. A Dinuclear Persulfide-Bridged Ruthenium Compound Is a Hypoxia-Selective Hydrogen Sulfide (H_2S) Donor. *Angew. Chem. Int. Ed.* **2021**, *60*, 1588–1592. https://doi.org/10.1002/anie.202012620.
(57) Li, A.; Turro, C.; Kodanko, J. J. Ru(II) Polypyridyl Complexes Derived from Tetradentate Ancillary Ligands for Effective Photocaging. *Acc. Chem. Res.* **2018**, *51*, 1415–1421. https://doi.org/10.1021/acs.accounts.8b00066.
(58) Bonnet, S. Ruthenium-Based Photoactivated Chemotherapy. *J. Am. Chem. Soc.* **2023**, *145*, 23397–23415. https://doi.org/10.1021/jacs.3c01135.

(59) Viala, C.; Coudret, C. An Expeditious Route to *Cis*-Ru(Bpy)$_2$Cl$_2$ (Bpy = 2,2′-Bipyridine) Using Carbohydrates as Reducers. *Inorg. Chim. Acta* **2006**, *359*, 984–989. https://doi.org/10.1016/j.ica.2005.07.019.
(60) Sullivan, B. P.; Salmon, D. J.; Meyer, T. J. Mixed Phosphine 2,2'-Bipyridine Complexes of Ruthenium. *Inorg. Chem.* **1978**, *17*, 3334–3341. https://doi.org/10.1021/ic50190a006.
(61) Jain, V. K.; Jakkal, V. S. Synthesis and Characterization of Areneruthenium(II) Dialkyldithiophosphate Complexes: Single Crystal Structure of [Ru{SSP(OEt)$_2$}(η^6-*p*-Cymene)(PPh$_3$)][BPh$_4$]. *J. Organomet. Chem.* **1996**, *515*, 81–87. https://doi.org/10.1016/0022-328X(95)06062-2.
(62) Raston, C. L.; White, A. H. Structural Studies in the Ruthenium–Dithiocarbamate System. Part II. Crystal Structures of Two Salts of the [Ru$_2$(Dtc)$_5$]$^+$ Cation, One Containing the [Ru$_2$Cl$_6$]$^{2-}$ Anion. *J. Chem. Soc. Dalton Trans.* **1975**, 2410–2418. https://doi.org/10.1039/DT9750002410.
(63) Wang, X.-Y.; Li, Y.; Ma, Q.; Zhang, Q.-F. Ruthenium Complexes with Dithiophosphonates [Ar(RO)PS$_2$]$^-$ and [Fc(RO)PS$_2$]$^-$ (Ar = *p*-CH$_3$OC$_6$H$_4$, Fc = Fe(η^5-C$_5$H$_4$)(η^5-C$_5$H$_5$)). *Organometallics* **2010**, *29*, 2752–2760. https://doi.org/10.1021/om100209k.
(64) Leverrier, A.; Hilf, M.; Raynaud, F.; Deschamps, P.; Roussel, P.; Tomas, A.; Galardon, E. Synthesis and Anti-Proliferative Activities of Ruthenium Complexes Containing the Hydrogen Sulfide-Releasing Ligand GYY4137. *J. Organomet. Chem.* **2017**, *843*, 26–31. https://doi.org/10.1016/j.jorganchem.2017.05.028.
(67) Ketkaew, R.; Tantirungrotechai, Y.; Harding, P.; Chastanet, G.; Guionneau, P.; Marchivie, M.; Harding, D. J. OctaDist: A Tool for Calculating Distortion Parameters in Spin Crossover and Coordination Complexes. *Dalton Trans.* **2021**, *50*, 1086–1096. https://doi.org/10.1039/D0DT03988H.
(68) Wachter, E.; Heidary, D. K.; Howerton, B. S.; Parkin, S.; Glazer, E. C. Light-Activated Ruthenium Complexes Photobind DNA and Are Cytotoxic in the Photodynamic Therapy Window. *Chem. Commun.* **2012**, *48*, 9649–9651. https://doi.org/10.1039/C2CC33359G.
(69) Macrae, C. F.; Sovago, I.; Cottrell, S. J.; Galek, P. T. A.; McCabe, P.; Pidcock, E.; Platings, M.; Shields, G. P.; Stevens, J. S.; Towler, M.; Wood, P. A. Mercury 4.0: From Visualization to Analysis, Design and Prediction. *J. Appl. Crystallogr.* **2020**, *53*, 226–235. https://doi.org/10.1107/S1600576719014092.
(68) Lawrence, M. A. W.; Bullock, J. L.; Holder, A. A. Basic Coordination Chemistry of Ruthenium. In *Ruthenium Complexes*; John Wiley & Sons, Ltd, 2018; pp 25–41. https://doi.org/10.1002/9783527695225.ch2.
(71) Marcolongo, J. P.; Schmidt, J.; Levin, N.; Slep, L. D. A Chemometric Approach for Determining the Reaction Quantum Yields in Consecutive Photochemical Processes. *Phys. Chem. Chem. Phys.* **2017**, *19*, 21373–21381. https://doi.org/10.1039/C7CP03619A.
(72) Crutchley, R. J.; Lever, A. B. P. Comparative Chemistry of Bipyrazyl and Bipyridyl Metal Complexes: Spectroscopy, Electrochemistry and Photoanation. *Inorg. Chem.* **1982**, *21*, 2276–2282. https://doi.org/10.1021/ic00136a030.
(73) Durham, B.; Caspar, J. V.; Nagle, J. K.; Meyer, T. J. Photochemistry of Tris(2,2'-Bipyridine)Ruthenium(2+) Ion. *J. Am. Chem. Soc.* **1982**, *104*, 4803–4810. https://doi.org/10.1021/ja00382a012.
(74) Van Houten, J.; Watts, R. J. Photochemistry of Tris(2,2'-Bipyridyl)Ruthenium(II) in Aqueous Solutions. *Inorg. Chem.* **1978**, *17*, 3381–3385. https://doi.org/10.1021/ic50190a016.
(73) Frisch, M. J.; Trucks, G. W.; Schlegel, H. B.; Scuseria, G. E.; Robb, M. A.; Cheeseman, J. R.; Scalmani, G.; Barone, V.; Mennucci, B.; Petersson, G. A.; Nakatsuji, H.; Caricato, M.; Li, X.; Hratchian, H. P.; Izmaylov, A. F.; Bloino, J.; Zheng, G.; Sonnenberg, J. L.; Hada, M.; Ehara, M.; Toyota, K.; Fukuda, R.; Hasegawa, J.; Ishida, M.; Nakajima, T.; Honda, Y.; Kitao, O.; Nakai, H.; Vreven, T.; Montgomery, J. A., Jr.; Peralta, J. E.; Ogliaro, F.; Bearpark, M.; Heyd, J. J.; Brothers,

E.; Kudin, K. N.; Staroverov, V. N.; Kobayashi, R.; Normand, J.; Raghavachari, K.; Rendell, A.; Burant, J. C.; Iyengar, S. S.; Tomasi, J.; Cossi, M.; Rega, N.; Millam, J. M.; Klene, M.; Knox, J. E.; Cross, J. B.; Bakken, V.; Adamo, C.; Jaramillo, J.; Gomperts, R.; Stratmann, R. E.; Yazyev, O.; Austin, A. J.; Cammi, R.; Pomelli, C.; Ochterski, J. W.; Martin, R. L.; Morokuma, K.; Zakrzewski, V. G.; Voth, G. A.; Salvador, P.; Dannenberg, J. J.; Dapprich, S.; Daniels, A. D.; Farkas, Ö .; Foresman, J. B.; Ortiz, J. V.; Cioslowski, J.; Fox, D. J. Gaussian 09, Revision D. 01; Gaussian, Inc.: Wallingford, CT, 2009. (76) Adamo, C.; Barone, V. Toward Reliable Density Functional Methods without Adjustable Parameters: The PBE0 Model. *J. Chem. Phys.* **1999**, *110*, 6158–6170. https://doi.org/10.1063/1.478522.

(75) Hariharan, P. C.; Pople, J. A. The Influence of Polarization Functions on Molecular Orbital Hydrogenation Energies. *Theor. Chim. Acta* **1973**, *28*, 213–222. https://doi.org/10.1007/BF00533485.

(76) Hehre, W. J.; Ditchfield, R.; Pople, J. A. Self—Consistent Molecular Orbital Methods. XII. Further Extensions of Gaussian—Type Basis Sets for Use in Molecular Orbital Studies of Organic Molecules. *J. Chem. Phys.* **1972**, *56*, 2257–2261. https://doi.org/10.1063/1.1677527.

(79) Marenich, A. V.; Cramer, C. J.; Truhlar, D. G. Universal Solvation Model Based on Solute Electron Density and on a Continuum Model of the Solvent Defined by the Bulk Dielectric Constant and Atomic Surface Tensions. *J. Phys. Chem. B* **2009**, *113*, 6378–6396. https://doi.org/10.1021/jp810292n.

(80) Knoll, J. D.; Albani, B. A.; Durr, C. B.; Turro, C. Unusually Efficient Pyridine Photodissociation from Ru(II) Complexes with Sterically Bulky Bidentate Ancillary Ligands. *J. Phys. Chem. A* **2014**, *118*, 10603–10610. https://doi.org/10.1021/jp5057732.

(81) Knoll, J. D.; Albani, B. A.; Turro, C. New Ru(II) Complexes for Dual Photoreactivity: Ligand Exchange and $^1O_2$ Generation. *Acc. Chem. Res.* **2015**, *48*, 2280–2287. https://doi.org/10.1021/acs.accounts.5b00227.

(80) Chatterjee, P.; Verma, M.; Sonkar, A. K.; Saha, A.; Mishra, R.; Sivakumar, S.; Patra, A. K. A Water-Soluble Photolabile Ruthenium(II) Complex with a Terpyridyl-Dicarboxylate Ligand: Photocytotoxicity Triggered by Structural Strain. *Inorg. Chem. Front.* **2025**, *12* (24), 8288–8303. https://doi.org/10.1039/D5QI01110H.

(83) Tachiyashiki, S.; Ikezawa, H.; Mizumachi, K. Identification of an Intermediate of the Photosubstitution of a Ruthenium(II) Diimine Complex with a Monodentate Chelating Ligand: ^{1}H NMR and HPLC Evidence. *Inorg. Chem.* **1994**, *33*, 623–625. https://doi.org/10.1021/ic00082a001.

(84) Welby, C. E.; Armitage, G. K.; Bartley, H.; Wilkinson, A.; Sinopoli, A.; Uppal, B. S.; Rice, C. R.; Elliott, P. I. P. Photochemistry of Ru^{II} 4,4′-Bi-1,2,3-Triazolyl (Btz) Complexes: Crystallographic Characterization of the Photoreactive Ligand-Loss Intermediate Trans-[Ru(Bpy)(κ^2-Btz)(κ^1-Btz)(NCMe)]$^{2+}$. *Chem. Eur. J.* **2014**, *20*, 8467–8476. https://doi.org/10.1002/chem.201402354.

(85) Welby, C. E.; Rice, C. R.; Elliott, P. I. P. Unambiguous Characterization of a Photoreactive Ligand-Loss Intermediate. *Angew. Chem. Int. Ed.* **2013**, *52*, 10826–10829. https://doi.org/10.1002/anie.201304219.

(86) Durham, B.; Caspar, J. V.; Nagle, J. K.; Meyer, T. J. Photochemistry of Tris(2,2'-Bipyridine)Ruthenium(2+) Ion. *J. Am. Chem. Soc.* **1982**, *104*, 4803–4810. https://doi.org/10.1021/ja00382a012.

(87) Garner, R. N.; Joyce, L. E.; Turro, C. Effect of Electronic Structure on the Photoinduced Ligand Exchange of Ru(II) Polypyridine Complexes. *Inorg. Chem.* **2011**, *50*, 4384–4391. https://doi.org/10.1021/ic102482c.

(88) Meijer, M. S.; Bonnet, S. Diastereoselective Synthesis and Two-Step Photocleavage of Ruthenium Polypyridyl Complexes Bearing a Bis(Thioether) Ligand. *Inorg. Chem.* **2019**, *58*, 11689–11698. https://doi.org/10.1021/acs.inorgchem.9b01669.

(89) Askes, S. H. C.; Meijer, M. S.; Bouwens, T.; Landman, I.; Bonnet, S. Red Light Activation of Ru(II) Polypyridyl Prodrugs via Triplet-Triplet Annihilation Upconversion: Feasibility in Air and through Meat. *Molecules* **2016**, *21*, 1460. https://doi.org/10.3390/molecules21111460.
(90) Hancock, R. D. Chelate Ring Size and Metal Ion Selection. The Basis of Selectivity for Metal Ions in Open-Chain Ligands and Macrocycles. *J. Chem. Educ.* **1992**, *69*, 615. https://doi.org/10.1021/ed069p615.
(89) Tachiyashiki, S.; Mizumachi, K. Mechanisms of the Photosubstitution of Ruthenium(II) Polypyridine Complexes: Formation of an Intermediate with a Monodentate Polypyridine Ligand and Its Reactions. *Coord. Chem. Rev.* **1994**, *132*, 113–120. https://doi.org/10.1016/0010-8545(94)80030-8.
(91) Hakkennes, M. L. A.; Regeni, I.; Husiev, Y.; Andreeva, V. D.; Siegler, M. A.; Buda, F.; Bonnet, S. Structure over States: Planarity, Not Energy, Dictates Photoactivation in Ru(II) PACT Agents. *J. Am. Chem. Soc.* **2025**, *147*, 35767–35787. https://doi.org/10.1021/jacs.5c12226.
(92) Sheldrick, G. M. A Short History of SHELX. *Acta Crystallogr. A* **2008**, *64*, 112–122. https://doi.org/10.1107/S0108767307043930.
(93) Sheldrick, G. M. Crystal Structure Refinement with SHELXL. *Acta Crystallogr. Sect. C Struct. Chem.* **2015**, *71*, 3–8. https://doi.org/10.1107/S2053229614024218.
(94) Müller, P. Practical Suggestions for Better Crystal Structures. *Crystallogr. Rev.* **2009**, *15*, 57–83. https://doi.org/10.1080/08893110802547240.
(95) Pinnick, D. V.; Durham, B. Photosubstitution Reactions of $Ru(Bpy)_2XY^{n+}$ Complexes. *Inorg. Chem.* **1984**, *23*, 1440–1445. https://doi.org/10.1021/ic00178a028.
(96) Liu, Y.; Turner, D. B.; Singh, T. N.; Angeles-Boza, A. M.; Chouai, A.; Dunbar, K. R.; Turro, C. Ultrafast Ligand Exchange: Detection of a Pentacoordinate Ru(II) Intermediate and Product Formation. *J. Am. Chem. Soc.* **2009**, *131*, 26–27. https://doi.org/10.1021/ja806860w.
(97) Perdew, J. P.; Burke, K.; Ernzerhof, M. Generalized Gradient Approximation Made Simple.*Phys. Rev. Lett.* **1997**, *78*, 1396–1396. https://doi.org/10.1103/PhysRevLett.78.1396.
(98) Ernzerhof, M.; Scuseria, G. E. Assessment of the Perdew–Burke–Ernzerhof Exchange-Correlation Functional. *J. Chem. Phys.* **1999**, *110*, 5029–5036. https://doi.org/10.1063/1.478401.
(99) Hay, P. J.; Wadt, W. R. Ab Initio Effective Core Potentials for Molecular Calculations. Potentials for K to Au Including the Outermost Core Orbitals. *J. Chem. Phys.* **1985**, *82*, 299–310. https://doi.org/10.1063/1.448975.

For Table of Contents Only